



HOKKAIDO UNIVERSITY

Title	Source Parameters and Rupture Mechanism of Deep-Focus Earthquakes
Author(s)	SASATANI, Tsutomu
Citation	Journal of the Faculty of Science, Hokkaido University. Series 7, Geophysics, 6(2), 301-384
Issue Date	1980-05-31
Doc URL	https://hdl.handle.net/2115/8720
Type	departmental bulletin paper
File Information	6(2)_p301-384.pdf



Source Parameters and Rupture Mechanism of Deep-Focus Earthquakes

Tsutomu SASATANI

(Received Oct. 15, 1979)

Abstract

One problem in studying source parameters of deep-focus earthquakes is the difficulty in determining source area and rupture mode because most of the methods for shallow events break down. In this study, the source area and rupture mode are determined from the aftershock distribution as well as through analyses of seismic body waves in the time domain. Synthetic body waves are compared with the deconvolved source time functions of P waves and with the observed seismograms of pP and S waves to obtain the source parameters. The reliable source parameters are obtained for four deep-focus earthquakes (three events in the Tonga arc and one event in the Kurile arc) with various focal depths. The following characteristics of the source parameters of deep-focus earthquakes are drawn from the results obtained in this study and those obtained by the other authors: the stress drops being larger than those of shallow earthquakes increase simply with focal depths and reach the order of magnitude of kilobars at depths of about 600 km; the rupture velocities are less than S wave velocity at a region around the focus, that is, 70 to 80% of the S wave velocity; of two nodal planes the steeply dipping one gives the fault plane whose dimension is 20 to 30 km at most. In the Tonga arc, the sense of fault movements during deep-focus earthquakes is found to be consistent with the sense of deformation of the descending lithosphere.

The investigation on the wave-form complexity of body wave seismograms of deep-focus earthquakes shows that the wave-form complexity is apparently caused by the earthquake source such as the multiple shock with a remarkably short time interval and that the multiple shocks occur very frequently in the deep seismic zone. The relative location of the first and subsequent shocks and the apparent rupture velocity are obtained for eighteen multiple shocks. The multiplets which include not only the multiple shock but also deep aftershocks are classified into four types depending on the relative location, the apparent rupture velocity, and the source dimension of the first shock. The four types are as follows: TYPE 1A, aftershocks occurring near the fault plane of the main shock; TYPE 1B, aftershocks occurring considerably apart from the fault plane of the main shock; TYPE 2A, the multiple shock triggered by the stress disturbance due to the rupture propagation of the first shock; TYPE 2B, the multiple shock triggered by the stress disturbance due to S wave radiated from the first shock. For occurrence of the multiplets, TYPE 1B and TYPE 2B are the frequent types. The stress disturbance due to S wave pulse that triggers the subsequent shock (TYPE 2B) is estimated to be several bars at most, from

computing strain seismograms. The inhomogeneous distribution of the initial stress and material strength is considered to play an important role in the rupture process of each type. This consideration indicates that the stress concentration at the focal region is quite limited in space in accordance with the large stress drop and the small source dimension of deep-focus earthquakes.

1. Introduction

The occurrence of earthquakes is understood as the consequence of a sudden release of strain energy stored up in a region of the earth's crust and mantle. A mode of the strain release or a source process is regulated by the physical properties of material and the dynamic process in the earth. Thus studies of the source process of earthquakes have revealed the physical properties and dynamic process in the earth's crust or mantle.

The deep-focus earthquakes occur in a region limited in and around island arcs and the spatial distribution of these earthquakes forms a seismic zone about 100 km thick dipping from a region around the trench to depths of several hundred kilometers in the upper mantle (Wadati¹; Honda²); Gutenberg and Richter³); Sykes⁴); Katsumata⁵); Utsu^{6,7})). The seismic zone is characterized by low attenuation (high Q) and high velocity (high V) of seismic waves as compared with the normal upper mantle at comparable depths (Utsu^{6,8}); Oliver and Isacks⁹)). In the plate tectonics hypothesis, the seismic zone is taken as a lithosphere which descends into the mantle (Isacks et al.¹⁰); Isacks and Molnar¹¹)).

Studies of the radiation pattern of seismic waves have revealed that a double-couple force system is the most pertinent to the interpretation of the observed radiation pattern (Honda^{2,12}); Stauder and Bollinger¹³); Ichikawa¹⁴); Isacks and Molnar¹¹)). In addition, it was also derived that one of the axes of compression and tension for the double-couple force system, which provide the direction of the earthquake-generating stresses, is approximately parallel to the dip of the seismic zone (e.g., Honda¹²); Isacks and Molnar¹¹)).

The static characteristics such as the seismicity and the direction of the earthquake-generating stresses for deep-focus earthquakes have been studied in detail in the different island arcs (e.g., Isacks and Molnar¹¹)). However, the physical properties such as the state of stress in the focal region, as well as the characteristics of rupture process of these earthquakes have never been clarified. To clarify these is the main purpose of the present study.

Recently the source process of earthquakes and the source parameters such as seismic moment, source area, average dislocation and stress drop

have been obtained for many shallow and deep-focus earthquakes through analyses of the geodetic and/or seismic data (Aki¹⁵); Kanamori^{16,17}); Abe^{18,19,20}); Teng and Ben-Menahem²¹); Berckhemer and Jacob²²); Bollinger²³); Khattri²⁴); Mikumo^{25,26,27}); Chandra²⁸); Fukao^{29,30}); Wyss³¹); Wyss and Molnar³²); Linde and Sacks³³); Koyama^{34,35}); Sasatani^{36,37}). However, for deep-focus earthquakes some confusion exists in source parameters obtained; for example, stress drops have been determined over the wide range from several bars (Wyss and Molnar³²); Linde and Sacks³³) to several hundred bars (Fukao³⁰); Sasatani^{36,37}). One problem in studying source parameters of deep-focus earthquakes is the difficulty in determining source area and rupture mode because most of the methods for shallow earthquakes break down. This may be one of causes of above confusion. In this paper, the source area and rupture mode are determined from the aftershock distribution as well as through analyses of seismic body waves. Synthetic body waves are computed for the fault model determined and are compared with observed body waves to obtain reliable source parameters. In chapter 2, source parameters of four deep-focus earthquakes (three events in the Tonga arc and one event in the Kurile arc) are obtained. The physical properties of the focal region will be discussed on the basis of the results obtained.

Determination of the fault plane provides information about the sense of fault movements during earthquakes. The sense of fault movement is closely related to dynamic process in the earth's crust or mantle. At the end of chapter 2, we shall briefly discuss about the dynamic process within the descending lithosphere on the basis of fault movements during earthquakes, especially about the relation between the sense of fault movements and the sense of deformation of the lithosphere.

The nature of spatial and temporal clustering of earthquakes have long been one of the main objects of seismological studies in connection with the process of earthquake generation. The foreshocks, aftershocks and earthquake swarms are representative of this nature. Mogi³⁸) showed, on the basis of the results from laboratory experiments on fracturing of rocks, that the nature of the clustering of earthquakes is closely related to the degree of heterogeneity or fracturing of rocks and to the stress concentration in the focal region.

There is a distinct kind of the clustering of earthquakes from the foreshocks, aftershocks and earthquake swarms; that is, the clustering of a few earthquakes occurring successively at a remarkably short time interval of several seconds

(Miyamura et al.³⁹); Isacks et al.⁴⁰); Oike⁴¹); Fukao³⁰); Gupta and Rostogi⁴²); Fukao and Furumoto⁴³); Sasatani³⁷); Chung and Kanamori⁴⁴). Here we term these earthquakes a multiple shock as used by Isacks et al.⁴⁰. The multiple shock is recognized by the waveform complexity of seismic body waves. Although triggering of earthquakes by stress disturbance due to the rupture propagation or due to S wave has been proposed to explain the multiple shocks, the mechanism of the multiple shocks and its implication relating to physical properties of the focal region have never been clarified. In chapter 3, we obtain the relative location of the first and subsequent shocks, and the apparent rupture velocity for eighteen multiple shocks. The multiplets which include not only the multiple shocks with a remarkably short time interval but also deep aftershocks are classified into four types depending on the relative location, the apparent rupture velocity, and the source dimension of the first shock. In the classification, the source parameters obtained in chapter 2 are used effectively. The mechanism of each type of the multiple shocks and its tectonic implications are also discussed. It will be shown that the inhomogeneous distribution of the initial stress and material strength plays an important role in the rupture process of each type.

2. Source parameters of deep-focus earthquakes

2.1 Method of analysis

In this section, we describe the essential theories to analyze seismic body waves and to determine the source parameters.

Deconvolution of seismic body waves

If the earth is idealized as a linear system, the observed seismogram $g(t)$ can be represented by a convolution integral as follows (Berckhemer and Jacob²³); Fukao³⁰):

$$g(t) = \int_{-\infty}^{+\infty} h(\tau) f(t-\tau) d\tau \quad (1)$$

where $h(t)$ is the impulse response of the transmitting system which consists of the earth and seismograph, and $f(t)$ is the source time function. The source time function $f(t)$ is, therefore, given by the deconvolution of $g(t)$:

$$F(\omega) = G(\omega)/H(\omega) \quad (2)$$

$$f(t) = \frac{1}{2\pi} \int_{-\infty}^{+\infty} F(\omega) e^{i\omega t} d\omega \tag{3}$$

where $F(\omega)$, $G(\omega)$ and $H(\omega)$ are the Fourier transforms of $f(t)$, $g(t)$ and $h(t)$, respectively. The source time function, which is obtained by eliminating the influence of the transmitting system, may be regarded as the displacement in a homogeneous and completely elastic, infinite medium (Berckhemer and Jacob²²).

According to Teng and Ben-Menahem²¹), $H(\omega)$ is given by

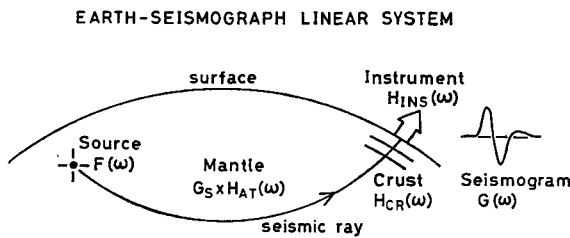
$$H(\omega) = G_s \cdot H_{AT}(\omega) \cdot H_{CR}(\omega) \cdot H_{INS}(\omega) \tag{4}$$

where G_s is the geometrical spreading factor which is independent of the frequency, and $H_{AT}(\omega)$, $H_{CR}(\omega)$ and $H_{INS}(\omega)$ are the complex transfer functions for the attenuation in the mantle, the layered crust and the instrument, respectively (Fig. 1). The geometrical spreading factor G_s is given by

$$G_s = \frac{1}{R} \sqrt{\frac{\rho_h V_h}{\rho_0 V_0} \frac{\sin i_h}{\sin \Delta \cos i_0} \left| \frac{di_h}{d\Delta} \right|} \tag{5}$$

(Honda¹²), where ρ is the density, V the velocity of seismic wave, i the incident angle, Δ the epicentral distance and R the radius of the earth. The subscripts h and o refer to the focus and the base of the crust, respectively. This factor is calculated for the velocity structure of Jeffreys⁴⁵ and the incident angles obtained from the extended distances by Hodgson and Storey⁴⁶).

The transfer function $H_{AT}(\omega)$ is computed using the following equation (Sato⁴⁷):



$$G(\omega) = G_S \times H_{AT}(\omega) \times H_{CR}(\omega) \times H_{INS}(\omega) \times F(\omega)$$

Fig. 1 Transmission of seismic body waves in the earth. The earth-seismograph linear system is assumed.

$$H_{AT}(\omega) = \exp(-\omega T_r/2\bar{Q}) \quad (6)$$

where T_r is the travel time, \bar{Q} the average specific quality factor along the ray path. For the Q structure, Model 11 of Mikumo and Kurita⁴⁸⁾ is used. The transfer function $H_{CR}(\omega)$ for the crustal structure as given in Table 1 is calculated by Haskell's method^{49),50)}.

Table 1 Crustal structure used for calculation of the crustal transfer function.

V_p km/s	V_s km/s	Density g/cm ³	Thickness km
6.10	3.50	2.70	11.0
6.40	3.68	2.90	9.0
6.70	3.94	2.90	18.0
8.15	4.75	3.30	—

In the present study, the seismograms obtained by the long-period seismograph of WWSSN (the World-Wide Standardized Seismograph Network) and by the strong motion seismograph of JMA (the Japan Meteorological Agency) are used. For the WWSSN long-period seismograph the transfer function $H_{INS}(\omega)$ is calculated according to Hagiwara's formula⁵¹⁾. Constants used in the calculation are such that $T_p=15$ sec, $T_g=100$ sec, $h_p=1.0$, $h_g=1.0$, $\sigma=0.15$ and $Mag=375-6000$, where T , h , σ , and Mag indicate the free period, the damping constant, the coupling constant and the magnification, respectively, and the subscripts p and g refer to the pendulum and the galvanometer. Constants of the strong motion seismograph (mechanical seismograph) are that $T_p=6$ sec (horizontal component), $\varepsilon=8$ and $Mag=1.0$, where ε is the damping ratio.

The actual procedure to obtain the source time function of P wave is as follows. The signal in the seismogram is digitized at an interval of 0.2 sec and applied to a time window of about 70 sec. Spectrum of the signal computed by a fast Fourier transform program (FFT) is corrected for the system transfer functions in the frequency domain, and is low-and high-cut filtered to remove the long-period drift and the short-period noise in the seismograms (Berckhemer and Jacob²²⁾). The inverse Fourier transform of this spectrum gives the P wave source time function. Figure 2 shows the comparison between the assumed and deconvolved source time functions and that between the assumed and synthetic seismograms. As shown in the figure a good agreement for both the source time functions and the seismograms is obtained. This

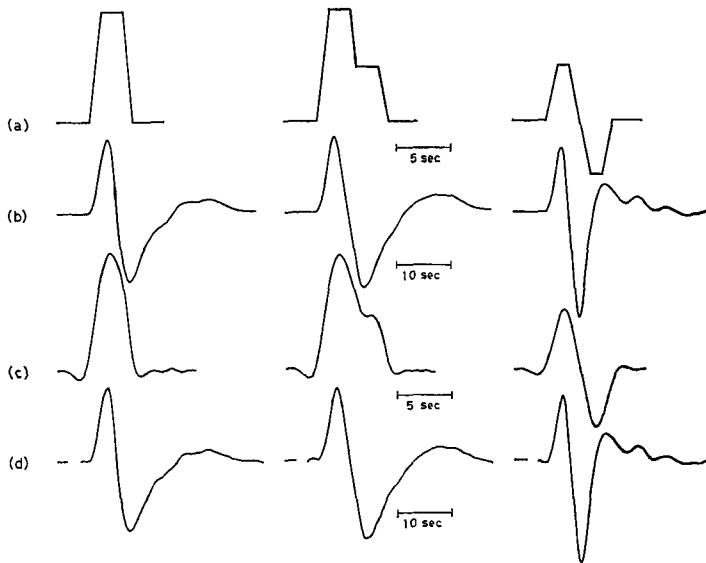


Fig. 2 Numerical studies of deconvolution of long-period P waves. (a): Source time functions assumed. (b): Synthetic seismograms obtained by convolution of (a) with the impulse response of the earth-seismograph linear system. (c): Source time functions obtained by deconvolution of (b). (d): Synthetic seismograms obtained by convolution of (c) with the impulse response of the earth-seismograph linear system. Compare (a) with (c), and (b) with (d), respectively.

agreement demonstrates that the low- and high-cut filtering stabilizes the inverse filter process with negligible errors as confirmed by Berckhemer and Jacob²²⁾ and Fukao³⁰⁾.

For the determination of source parameters, the synthetic wave form has been compared with the observed wave form either in the time domain (Fukao³⁰⁾; Sasatani³⁶⁾) or in the frequency domain (Khattri²⁴⁾; Wyss and Molnar²²⁾). In the frequency domain, it is difficult to observe how degree the individual source parameter affects the spectrum; for multiple shocks, it is also difficult to obtain the direct understanding of the time sequence and duration of transient pulses based on the spectrum. On the other hand, if the theoretical source time functions and seismograms are compared with the observed ones in the time domain, it is easy to investigate how degree the source parameters affect the source time functions and seismograms. In the present study, the source time functions are usually used to obtain the source

parameters, because the source time function is known as being much more sensitive to the source parameters than the seismogram (Sasatani³⁶). However, for pP and S waves the deconvolution technique provides no reliable source time function because of the waves with a low signal-to-noise ratio due to contamination by different waves. Therefore, for these waves the seismograms are used to obtain the source parameters.

Theoretical seismic body waves

Elastic displacements due to a simple faulting source in an infinite homogeneous medium have been discussed by a number of authors (e.g., Haskell^{52,53}; Berckhemer and Jacob²²); Hirasawa and Stauder⁵⁴; Savage^{55,56}). In principle, the faulting may be simulated by the superposition of source elements with time delay that is equivalent to the rupture propagation in the source area. For the calculation of the elastic displacement due to a faulting source, the methods given by Savage⁵⁶, Hirasawa and Stauder⁵⁴ and Haskell⁵³ are used.

According to Savage⁵⁶, the theoretical source time function $f_{p,s}(t)$ radiated from a fault with the arbitrary shape (see Fig. 3) in the far-field approximation is given by

$$f_{p,s}(t) = \frac{\mu R_{p,s}}{4\pi\rho V_{p,s}^3 r_0} V_r^2(t-r_0/V_{p,s}) H(t-r_0/V_{p,s}) \int \frac{D(b', \phi')}{q_{p,s}^2} d\phi' \quad (7)$$

$$q_{p,s} = 1 - (V_r/V_{p,s}) \sin \theta \cos(\phi' - \phi),$$

where μ is the rigidity, $R_{p,s}$ the radiation pattern coefficient for P and S waves associated with the equivalent force system, that is, the double-couple force system, $V_{p,s}$ the velocity of P and S waves, r_0 the distance from the source to the observation point (the point Obs., spherical polar coordinates r_0, θ, ϕ), V_r the rupture velocity, H the unit step function, and D the dislocation at the polar coordinates b' and ϕ' in the fault surface $z=0$. The integral is over all values of ϕ' in a region bounded by the fault surface through which the rupture propagates. The dislocation is assumed to occur instantaneously, that is, stepwise.

If the fault has rectangular shape as shown in Fig. 4, the source time function $f_{p,s}(t)$ in the far-field approximation is given by the method of Hirasawa and Stauder⁵⁴ as

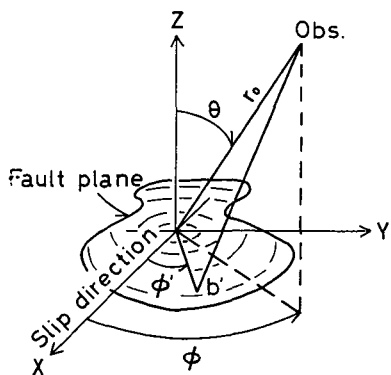


Fig. 3 Fault model of Savage⁵⁶⁾, and coordinate system and notations used in the calculation.

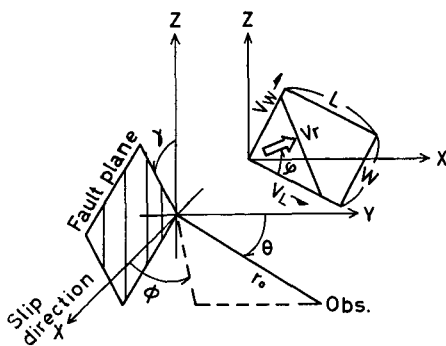


Fig. 4 Fault model of Hirasawa and Stauder⁵⁴⁾, and coordinate system and notations used in the calculation.

$$f_{p,s}(t) = \frac{M_0 R_{p,s}}{4\pi\rho V_{p,s}^3 r_0} s(t) \tag{8}$$

$$s(t) = \begin{cases} 1/2 |Y_{p,s}| & \text{for } |t| \leq |Y_{p,s}| - |X_{p,s}| \\ \frac{\mp t + |X_{p,s}| + |Y_{p,s}|}{4|X_{p,s}||Y_{p,s}|} & \text{for } \mp: t \geq 0 \\ 0 & \text{for } |t| \geq |Y_{p,s}| + |X_{p,s}| \end{cases}$$

$$X_{p,s} = \frac{W}{2} \left\{ \frac{1}{V_W} + \frac{1}{V_{p,s}} \sin \theta \sin (\phi - \gamma) \right\},$$

$$Y_{p,s} = \frac{L}{2} \left\{ \frac{1}{V_L} - \frac{1}{V_{p,s}} \sin \theta \cos (\phi - \gamma) \right\}$$

where M_0 is the total seismic moment (see equation (13)), L the fault length, W the fault width, V_L and V_W are the apparent rupture velocities along the L and W directions as defined by $V_L = V_r / \cos \phi$ and $V_W = V_r / \sin \phi$. The line segment W is inclined at the angle γ from the z -axis in the plane $y=0$. The point Obs. is the observation point. The instantaneous dislocation is here assumed. It should be noted that the above expression of $s(t)$ is given for

the case in which $|Y_{p,s}| \geq |X_{p,s}|$. If $|Y_{p,s}| \leq |X_{p,s}|$, $s(t)$ is obtained by interchange of $|Y_{p,s}|$ and $|X_{p,s}|$.

Equations (7) and (8) show that the pulse widths of the source time functions are of shortest time duration in the direction of fault propagation and of longest duration in the opposite direction (Fig. 5). In addition, these equations show that the amplitudes of the source time functions corrected for the radiation pattern coefficient are larger in the direction of fault propagation than in the opposite direction, while the area enclosed by a curve of the source time function (hatched area in Fig. 5) is constant in all of the direction (Savage⁵⁶). These variations in the source time function are herein designated as a "Doppler-type effect" in analogy with the electromagnetic and acoustic phenomena that result when there is relative motion between source and observer.

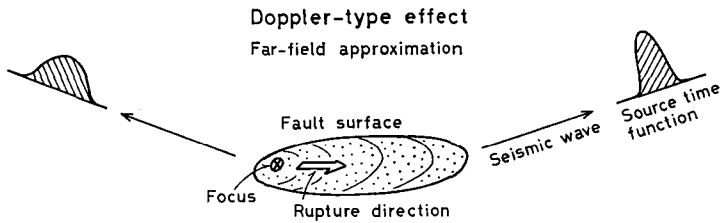


Fig. 5 Doppler-type effect of seismic body waves due to the rupture propagation (uni-lateral faulting).

In computing the dynamic near-field displacement, the integral expression given by Haskell (equations (3) and (4) in his paper⁵³) are numerically double-integrated over a fault surface on the assumption that the dislocation takes place simultaneously over the fault width W , that is, $V_W = \infty$ in Fig. 4, and propagates at a constant velocity V_r along the fault length L . The temporal variation of the dislocation is given as a ramp function of rise time τ , that is,

$$G(t) = \begin{cases} 0 & \text{for } t < 0 \\ t/\tau & \text{for } 0 \leq t \leq \tau \\ 1 & \text{for } t > \tau \end{cases} \quad (9)$$

$$D(t) = D_0 G(t)$$

where D_0 is the final dislocation.

The far-field source time function due to the time dependent dislocation such as a ramp function defined above is given by Savage⁵⁶):

$$f'_{p,s}(t) = \tau^{-1} \int_0^t f_{p,s}(t-t') [H(t') - H(t'-\tau)] dt' \quad (10)$$

where $f_{p,s}(t)$ is the source time function due to the instantaneous dislocation.

Substitution of these source time functions or displacements into equation (1) gives the theoretical seismograms. For S waves, SV- and SH-wave seismograms being computed are decomposed into NS-and EW-components by the rotation of axis (Sasatani⁵⁷).

The final step in the analysis is to compare the theoretical wave form with the observed one in order to deduce the dynamic source parameters such as the rupture velocity. The fitting of the theoretical wave form with the observed one has often been made with our eyes. In the present analysis, to judge the degree of the fitting between both wave forms statistically, the parameters R_f and R_g are introduced:

$$R_f = \frac{1}{N} \sum_i R_{f,i} \quad (11)$$

$$R_{f,i} = \frac{\sqrt{\sum_j (f_j^{\text{obs}} - f_j^{\text{th}})^2}}{\max(f_j^{\text{obs}})}$$

$$R_g = \frac{1}{N} \sum_i R_{g,i} \quad (12)$$

$$R_{g,i} = \frac{1}{\max(g_j^{\text{obs}})} \sqrt{\frac{\sum_j W_j (g_j^{\text{obs}} - g_j^{\text{th}})^2}{\sum_j W_j}}$$

where $R_{f,i}$ is a measure of the fitting for the source time function derived from the i -th station and $R_{g,i}$ is that for the seismogram at the i -th station. The terms f_j and g_j are amplitudes of the source time function and the seismogram at the time j , respectively. The superscripts obs and th refer to the observed and theoretical quantities. The sampling rate for these quantities is 0.2 sec for the source time function and 1 sec for the seismogram. For comparison of the seismograms, the peak amplitude of the theoretical seismogram is normalized to that of the observed one. R_f and R_g are the average of $R_{f,i}$ and $R_{g,i}$, respectively. N is the number of stations used.

W_j is the weighting function defined as

$$W_j = 1 \quad \text{for } t_0 \leq t_j \leq t_1, \\ = \cos^2 \theta_j \quad \text{for } t_1 \leq t_j \leq t_2$$

where

$$\theta_j = \frac{\pi}{2} (t_j - t_1) / (t_2 - t_1).$$

When the times t_0 , t_1 and t_2 are selected as shown in Fig. 7, the significant part of source process of the earthquake can be included safely in the first half-cycle of the waves. Figures 6 and 7 show an illustration of the observed wave form compared with the theoretical wave forms calculated for various rupture velocities. The dynamic source parameters are determined so as to make R_f and R_g minimum.

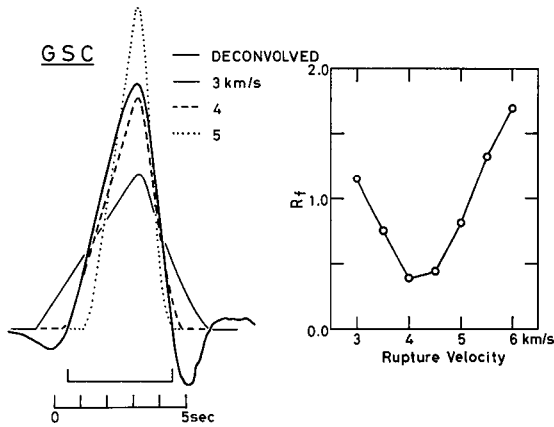


Fig. 6 Comparison of the deconvolved source time function with the theoretical source time functions for various rupture velocities. R_f is defined in the text.

Source parameters

Source parameters to be determined are total seismic moment M_0 , source area S , average dislocation \bar{D} , rise time of slip dislocation τ , stress drop $\Delta\sigma$ and rupture velocity V_r . From equations (7) and (8) total seismic moment M_0 can be obtained from the P wave source time function $f_p(t)$ by using the following equation (Berckhemer and Jacob²²):

$$M_0 = 4\pi\rho r_0 V_p^3 R_p^{-1} \int f_p(t) dt. \quad (13)$$

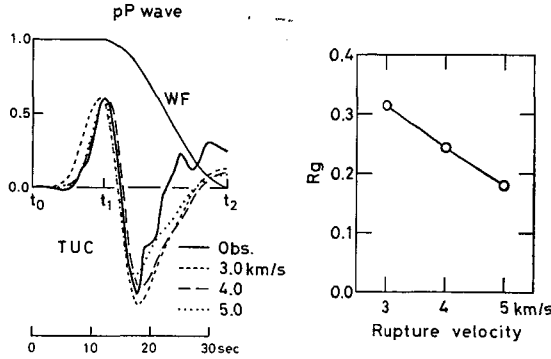


Fig. 7 Comparison of the observed seismogram of pP wave with the synthetic seismograms for various rupture velocities. WF is the weighting function. R_g is defined in the text.

Since the equivalence of the double-couple force system to the shear dislocation (Maruyama⁵⁸; Burridge and Knopoff⁵⁹) provides that the total seismic moment is related to the source area and the average dislocation (Aki¹⁵) as

$$M_0 = \mu \bar{D} S, \tag{14}$$

the average dislocation is given by

$$\bar{D} = M_0 / \mu S. \tag{15}$$

The stress drop, that is, the difference in stress before and after the earthquake is derived from the following equation (Eshelby⁶⁰):

$$\Delta\sigma = \frac{7}{16} \frac{M_0}{C^3} = \frac{7\pi}{16} \mu \frac{\bar{D}}{C} \tag{16}$$

where $C = (S/\pi)^{1/2}$ is the radius of a circular fault with area S to which the fault surface may be approximated for simplicity.

Although actual dislocations and rupture velocities may vary on regions of the fault surface in response to the initial stress field (Yamashita⁶¹; Auer and Berckhemer⁶²; Das and Aki⁶³), the source parameters averaged over the fault surface will be used in the present analysis. This is because of a difficulty in determining the dislocations and the rupture velocities as a function of points on the fault surface.

Effects due to the anomalous structure in the upper mantle beneath island arcs on the long-period waves

Utsu^{6),8)} showed the presence of the large scale anomalous structure in the upper mantle beneath island arc; a high Q and high velocity zone about 100 km thick dips from the vicinity of the trench to a depth of several hundred kilometers in the upper mantle on the continental side. Investigation of a ray tracing of seismic waves shows that rays going parallel to the dip of this anomalous structure provide not only anomalous travel times but also anomalous amplitudes (e.g., Davies and Julian⁶⁴⁾, Sleep⁶⁵⁾; see Fig. 8(b)). If this is true, the anomalous structure becomes a trouble in determining the source parameters. However, Sleep⁶⁵⁾ concluded that the anomalous structure gives no systematic effects to the waves at long-period, although this structure produces the shadow zone on the earth's surface for the waves at short-period. Here the amplitudes of long-period P waves obtained from the WWSSN records were investigated to confirm the Sleep's conclusion.

An intermediate-depth earthquake which occurred on May 22, 1972 in the Tonga arc was selected for this investigation. As shown in Figs. 8(a) and 8(b), the ray tracing for the intermediate-depth earthquake suggests that the shadow zone appears on the west of the Tonga arc (Sleep⁶⁵⁾). Figure 8(d) shows the observed amplitudes of long-period P waves. In order to interpret amplitude data, it is necessary to correct for variations in amplitude as the result of heterogeneities in the radiation pattern at the focus and as a result of systematic variations with epicentral distance (the geometrical spreading). Figure 8(e) shows the amplitudes corrected for the radiation pattern and the geometrical spreading. In Fig. 8(e), the amplitudes at stations in the southwest direction are somewhat reduced as suggested by the ray tracing. However, as mentioned earlier, the rupture propagation also gives variations in amplitude (the Doppler-type effect, see Fig. 5). Therefore, this effect must be removed from the amplitudes in order to investigate amplitude anomalies due to the anomalous structure. The total seismic moment as defined by equation (13) is independent of the rupture propagation (Berckhemer and Jacob²²⁾) so that the seismic moment can be considered as the most suitable quantity for this purpose. Figure 8(f) shows the total seismic moments obtained from the source time functions of P waves. It is clear that the total seismic moments are nearly the same at stations with various azimuths; that is, no shadow zone is observed. The amplitude reduction in the southwest direction in Fig. 8 (e) may be due to the Doppler-type effect.

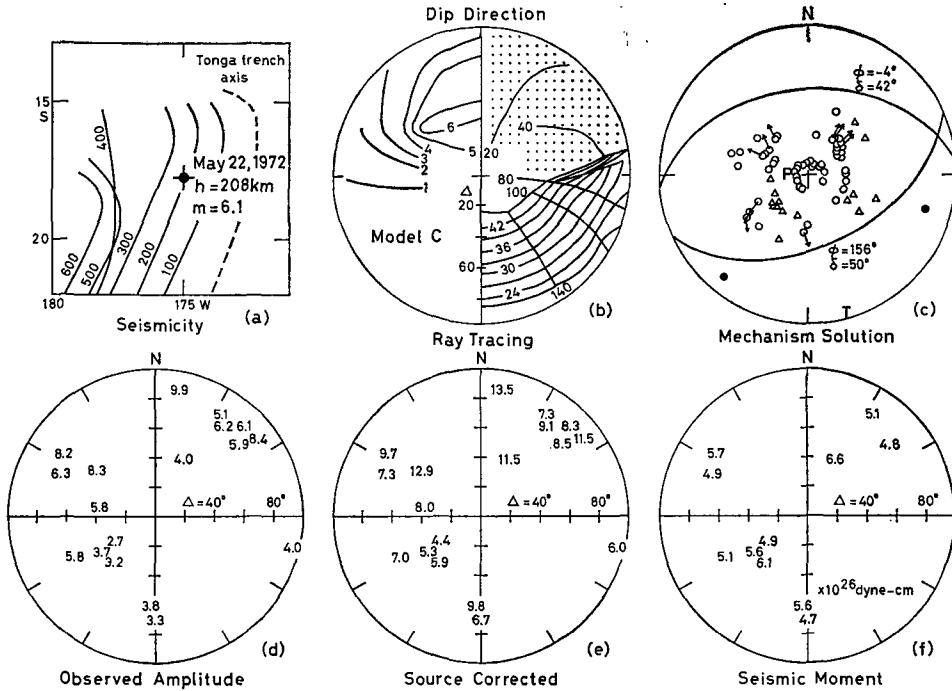


Fig. 8 (a) Map showing the iso-depth lines of deep-focus earthquakes in the northern part of the Tonga arc (Isacks and Molnar¹¹), and the epicenter of the earthquake studied. (b) Result for ray tracing from 200-km deep source in the Tonga arc (Sleep⁸⁵); c in his Fig. 6). Calculated travel-time residuals (advances positive) are plotted on the left of an equi-distance azimuthal projection about the source. Calculated initial ray parameters (initial take-off angles and initial take-off azimuths) for rays emerging on the projection are plotted on the right. The stippling indicates the area of significantly reduced amplitudes. (c) Focal mechanism solution for the earthquake of May 22, 1972. For symbols, see caption of Fig. 10. (d) Observed amplitudes of the WWSSN long-period seismograms ($Mag = 1500$), plotted on equi-distance azimuthal projection about the source. (e) Corrected amplitudes for the geometrical spreading and the radiation pattern. (f) Seismic moments obtained from the P wave source time functions.

In the following sections, it will be shown that the anomalous structure in the upper mantle gives no effect on determining the total seismic moment for most earthquakes. This and above evidences show that as far as long-period seismic waves are considered, effects due to the anomalous structure may be negligible, and that the Sleep's conclusion is correct.

2.2 *Three deep-focus earthquakes in the Tonga arc*

In this section and the following section, the source parameters are obtained for four deep-focus earthquakes ($m_b \geq 6.0$) with various focal depths. The procedure to obtain the source parameters is as follows. First the fault model is constructed on the basis of the aftershock distribution and the focal mechanism solution of the main shock. Next wave-form analysis of the seismic body waves is done in the time domain to confirm the fault model thus estimated and to obtain the source parameters. In the analysis, we use upgoing waves as well as downgoing waves to wide the azimuthal coverage of seismic wave radiation.

Three deep-focus earthquakes studied here are the west of Tonga earthquake of October 9, 1967 (abbreviated as 1967 event), the south of Fiji earthquake of March 30, 1972 (1972 event), and the south of Fiji earthquake of February 22, 1975 (1975 event). The number of aftershocks is four, six and only one for the 1967, 1972 and 1975 events, respectively.

Aftershocks and focal mechanism solutions

The hypocenters of the main shock and the large aftershocks ($m_b \geq 4.5$) were redetermined on the basis of the P times as reported in the seismological bulletins of the International Seismological Center (ISC). The Jeffreys-Bullen travel time table was used. We made the relocation by using P times from all stations with distance $\Delta \leq 100^\circ$, excluding those whose O-C (observed minus computed P time) exceed 4 sec. The hypocenters and the time sequence for each event are shown in Fig. 9 and Table 2. The aftershocks for the 1967 and 1972 events occur at relatively larger depths and in the area elongated in one direction; that is, in a northeast-southwest direction for the 1967 event, and in a north-northwest to south-southeast direction for the 1972 event except for Nos. 7 and 8. The only aftershock of the 1975 event is located deeper by about 50 km than the main shock.

As shown in Fig. 13(b), seismograms of P, pP and S waves of the 1972 event show the multiple arrivals. Since the second phases do not correspond to any of phases predicted by the travel time curves, this event can be regarded as a multiple shock, that is, a doublet (Sasatani⁶⁶). The amplitude of the seismic signals of the second shock is much larger than that of the first shock (Fig. 13(b)). This implies that the first shock is the foreshock and the second shock is just the main shock. The relative location and the difference in origin times of the foreshock and the main shock were determined from the

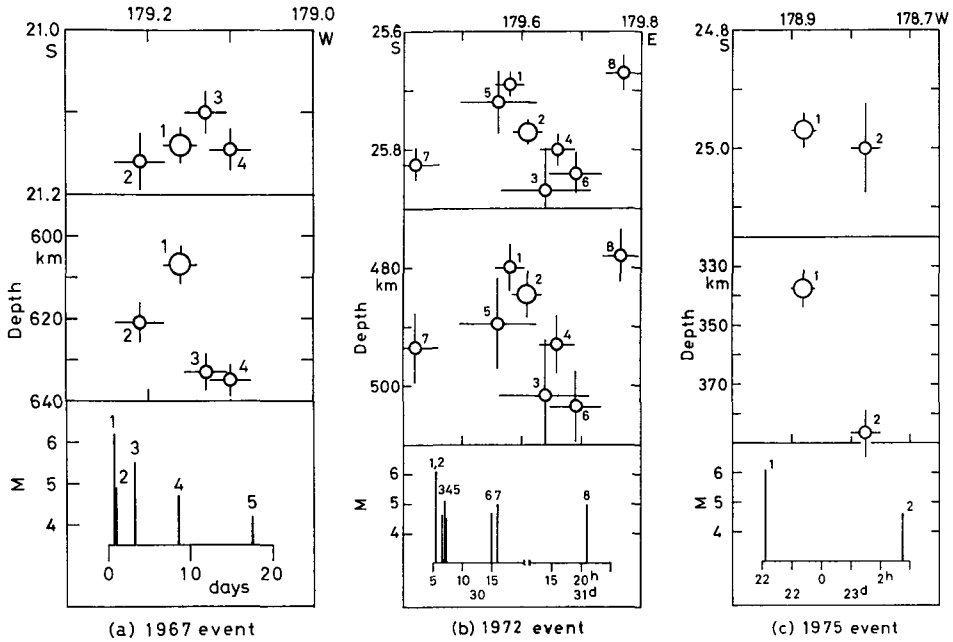


Fig. 9 Spatial distribution of the main shock and aftershocks. Large symbols indicate the main shock. The numbers refer to the earthquakes listed in Table 2.

multiple-shock analysis as mentioned in chapter 3. The solution gives: origin time difference=5.7 sec, spatial separation=10.4 km, and direction of the line element connecting the two foci, $(\phi, \delta)=(160^\circ, 64^\circ)$, where ϕ is the azimuth measured clockwise from the north and δ is the plunge angle measured from downward vertical (in detail, see chapter 3 and Sasatani⁶⁶). The hypocenter of the main shock of the 1972 event was determined in this way. We determine the source parameters for the main shock.

The focal mechanism solution for each main shock was determined on the basis of the first motions of P and pP waves and the polarization angles of S waves, obtained from the WWSSN long-period seismograms (Fig. 10). The standard deviation of the S wave polarization angles from the expected value is 10.6° for the 1967 event, 7.0° for the 1972 event, and 10.4° for the 1975 event. Isacks and Molnar¹¹) determined the mechanism solution for the 1967 event, which is similar to that determined here (Fig. 10(a)). The mechanism solution for the foreshock of the 1972 event was also determined

Table 2 Focal coordinates of the main shock and aftershocks for the Tonga earthquakes.

(a) 1967 event

No.	Date m d y	Origin time h m s	Lat. °S	Long. °W	Depth km	m_b	RMS sec
1	Oct. 09, 1967	17 21 46.1	21.14	179.16	607	6.2	0.99
2	Oct. 09, 1967	18 33 08.8	21.16	179.21	621	4.9	1.12
3	Oct. 12, 1967	06 35 06.6	21.10	179.13	633	5.5	1.07
4	Oct. 17, 1967	14 08 58.3	21.14	179.10	635	4.7	0.94

RMS=root mean square of the observed minus computed P times (O-C residuals).

(b) 1972 event

No.	Date m d y	Origin time h m s	Lat. °S	Long. °E	Depth km	m_b	RMS sec
1	Mar. 30, 1972	05 34 50.3	25.69	179.58	480	—	1.30
2*	Mar. 30, 1972	05 34 56.0	25.77	179.61	485	6.1	—
3	Mar. 30, 1972	06 47 24.1	25.87	179.64	502	4.6	1.57
4	Mar. 30, 1972	07 04 07.1	25.80	179.66	493	5.1	1.24
5	Mar. 30, 1972	07 23 56.4	25.72	179.56	490	4.5	1.09
6	Mar. 30, 1972	14 54 09.9	25.84	179.69	503	4.7	1.06
7	Mar. 30, 1972	15 58 01.5	25.83	179.42	494	5.0	1.23
8	Mar. 31, 1972	20 56 56.3	25.67	179.77	478	5.0	1.12

*, main shock

(c) 1975 event

No.	Date m d y	Origin time h m s	Lat. °S	Long. °W	Depth km	m_b	RMS sec
1	Feb. 22, 1975	22 04 33.7	24.97	178.88	338	6.1	1.26
2	Feb. 23, 1975	02 46 19.5	25.00	178.78	387	4.6	0.99

in the similar manner (Fig. 10(b)). This solution is somewhat different from that of the main shock (Fig. 10(c)).

One of two nodal planes of each main shock is nearly vertical and the other is nearly horizontal. Comparison of the spatial distribution of the aftershocks (Fig. 9) with the mechanism solution for the main shock (Fig. 10) shows that the aftershocks of the 1967 and 1975 events occur near the steeply dipping nodal plane of the main shock. For the 1972 event, the four aftershocks from No. 3 to No. 6 occurring in the early stage are located near the steeply dipping nodal plane of the main shock, while the other two aftershocks of Nos. 7 and 8 are located approximately on the other nodal plane. The

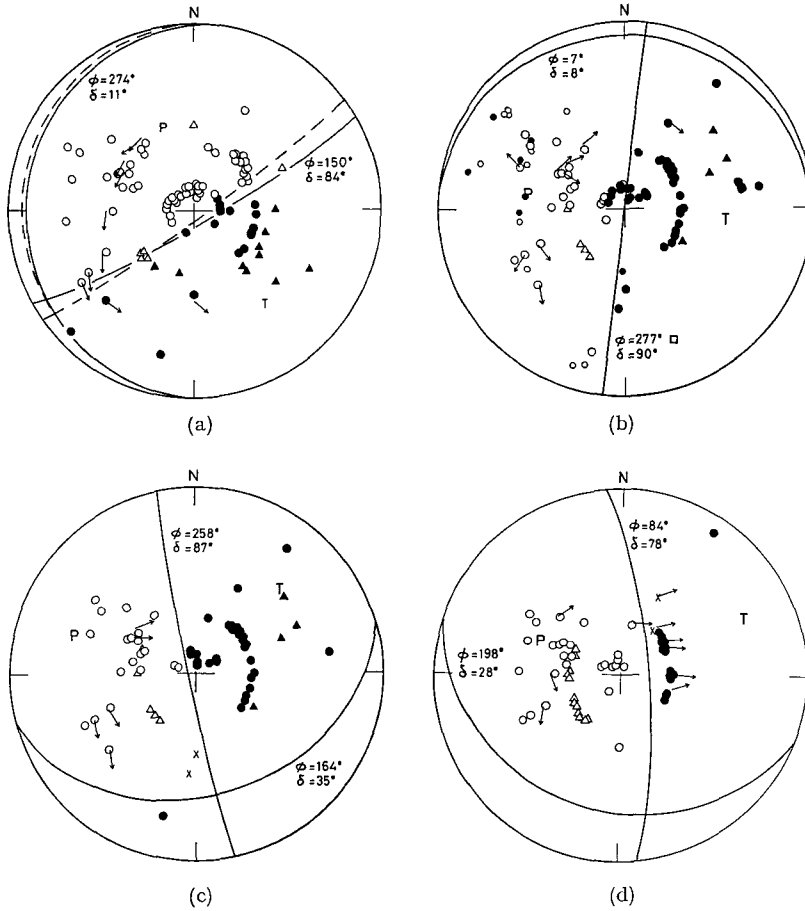


Fig. 10 Focal mechanism solutions: (a) Main shock of the 1967 event, (b) Foreshock of the 1972 event, (c) Main shock of the 1972 event, and (d) Main shock of the 1975 event. The first motions of P and pP waves are projected on the lower half of the focal sphere using equal-area projection. The closed symbols and open symbols indicate the compressions and dilatations, and circles and triangles refer to P and pP waves, respectively. Arrows indicate the S wave polarization angles. Crosses indicate stations judged to be near a nodal plane in the radiation pattern from the character of the signals. ϕ is the dip direction measured clockwise from the north and δ is the dip angle. P and T represent the axis of compression and the axis of tension, respectively. In (a), the dashed curves are nodal planes determined by Isacks and Molnar¹¹.

earlier aftershocks appear to be directly related to the generation of the fault plane of the main shock.

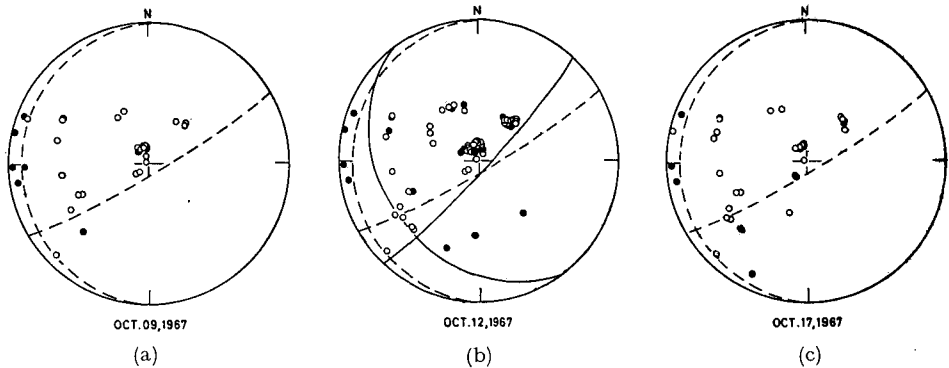


Fig. 11 Distribution of the first motions of P waves for the aftershocks of the 1967 event. Symbols are the same as in Fig. 10. The dashed curves are nodal planes of the main shock. The solid curves in (b) are the nodal planes determined by Isacks and Molnar¹¹⁾.

Figure 11 shows the distribution of the first motions of P waves for three large aftershocks of the 1967 event. These data were taken from the seismological bulletins of ISC. Since the number of the data is a few and the azimuthal distribution of the stations for the data is limited in a narrow range, the mechanism solutions for these aftershocks cannot be determined definitely. The distribution of the first motions for these aftershocks, however, is nearly the same as that for the main shock. This indicates that the stresses which generate the aftershocks are almost similar to those which generate the main shock. This similarity is not held apparently for the 1972 and 1975 events: compressions and dilatations are mixed in the radiation patterns for the aftershocks of these events. This mixture is probably due to the erroneous reading of the weak first motion which may be possible for such a small earthquake with magnitude less than about 5.0.

According to dislocation theory, one of the two nodal planes of the double-couple solution corresponds to the actual fault plane (Maruyama⁵⁸⁾), and after the generation of the fault plane the stresses similar to those which generate the fault plane will concentrate at and near the edge of the fault plane (Oike⁶⁷⁾; Rybicki⁶⁸⁾). Consequently, this theory predicts that the aftershocks occur near one of the nodal planes of the mechanism solution for the main shock, and that the mechanism solution for the aftershocks is nearly the same as that for the main shock. Evidences mentioned above coincide with this prediction approximately. From this consideration it may be concluded that the kinematic model of deep-focus earthquakes is the shear

faulting, that is, the slip dislocation, and that the fault plane of each main shock is the steeply dipping nodal plane.

The dislocation theory anticipates that aftershocks outline approximately the rupture area of the main shock. Thus we can assume the fault model of each main shock by enclosing the aftershocks. However, since the number of the aftershocks is not so many, we cannot determine the fault geometry decidedly. Two possible fault models were assumed for the 1967 and 1972 events (Figs. 12(a), 12(b)); the triangular (Model 1) and elliptical (Model 2) fault models for the 1967 event, and the rectangular (Model 1) and elliptical (Model 2) fault models for the 1972 event. For the 1975 event, since the number of the aftershock is only one, we assumed unavoidably that the fault geometry is elliptical as shown in Fig. 12(c). Five fault models will be assumed for this event in the next paragraph. Wave-form analysis of seismic body waves in the next paragraph will decide which of the fault models is more reliable for each event.

For the elliptical fault model, the ratio of the major semi-axis a to the minor semi-axis b is assumed as two, that is, $a/b=2$. This assumption may be supported by the evidences that the fault length is approximately twice the fault width for many shallow earthquakes (Kanamori and Anderson⁶⁹; Abe⁷⁰; Geller⁷¹).

The assumed fault models show that the rupture propagated uni-laterally downward from the focus of the main shock. The rupture mode of each fault model was assumed as represented in Fig. 12. For the triangular fault model, the rupture starts from an apex of the triangle and spreads uni-laterally at a constant rupture velocity until it has cover a triangular fault surface. The rupture front is a line parallel to a side opposite the apex. For the elliptical fault model, the rupture starts at a focus of the ellipse and spreads circularly at a constant rupture velocity (Savage⁵⁶). Finally for the rectangular fault model, the rupture starts at a corner of the rectangle and spreads at a constant rupture velocity. The apparent rupture velocity in the direction of the fault length is assumed to be the same as that in the direction of the fault width, that is, $V_L=V_W$ in Fig. 4. It is also assumed for all fault models that the dislocation is constant over the fault surface, and occurs step wise.

Analysis of P and pP waves

Figure 13 shows examples of the observed seismograms of P and pP waves for each event. As it is known that the pulse width of seismic wave is

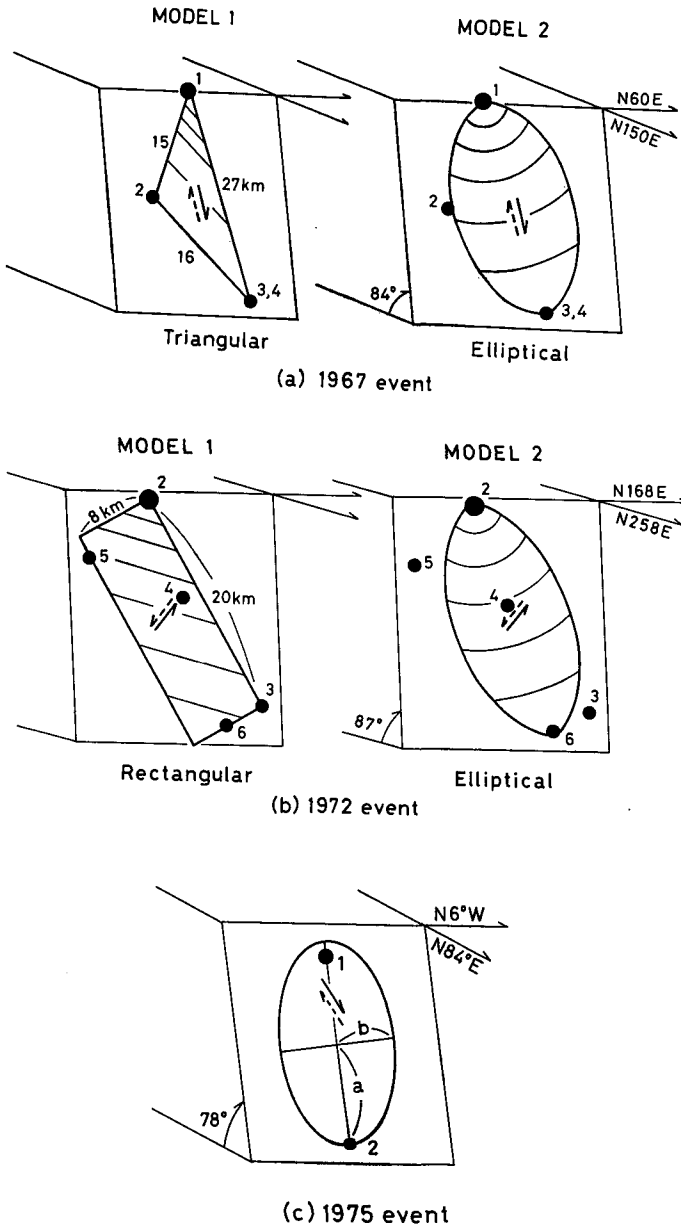


Fig. 12 Spatial distribution of the aftershocks over the fault plane and geometry of fault models assumed for each event. Double arrows indicate sense of shear displacement on the fault plane. Rupture front is shown by lines in the fault plane.

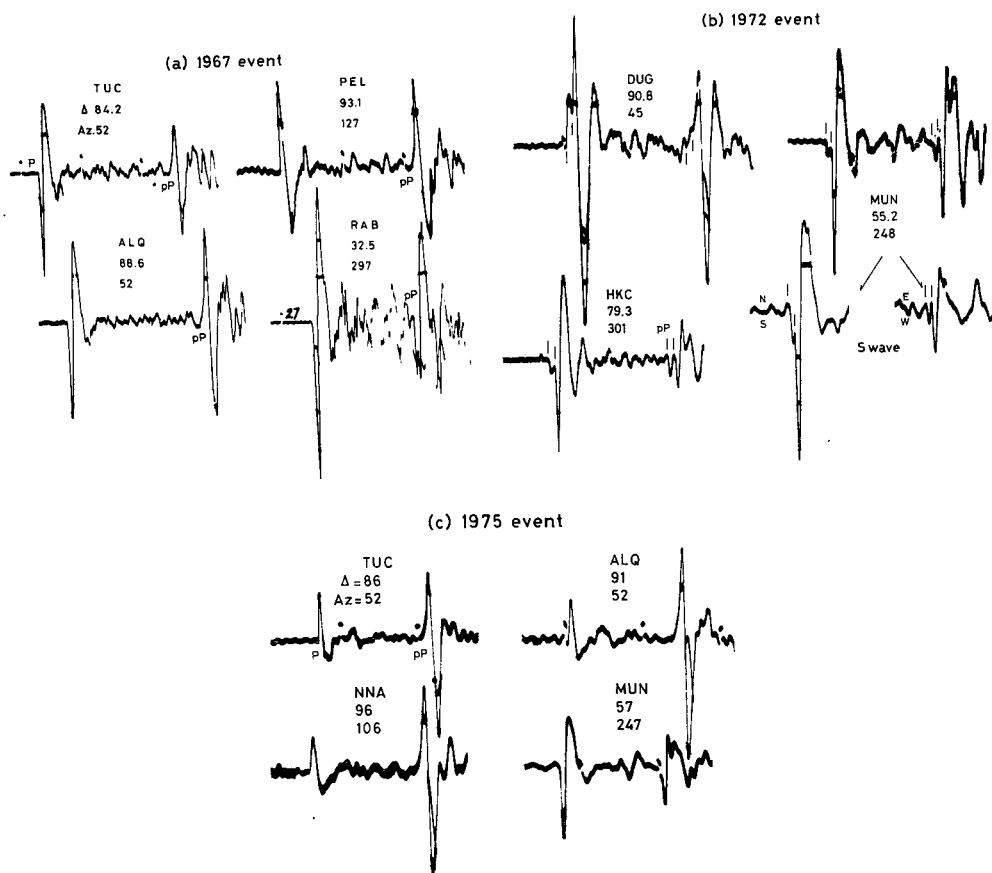


Fig. 13 WWSSN long-period seismograms (vertical component) of the Tonga deep-focus earthquakes studied.

reflected upon the duration of the first half-cycle of seismograms (the duration from wave initiation to the first zero-line crossing) (Bollinger²³); Sasatani⁷²), these seismograms show that the pulse width of pP wave is longer than that of P wave. This may be due to the difference between the ray paths for P and pP waves: pP wave travels through a region of the upper mantle with lower Q as compared with P wave. The difference of the ray paths produces the difference of the attenuation of the seismic waves. We examine the effect of the attenuation of seismic waves due to inelasticity.

The synthetic P wave seismograms were computed using equation (1) for the source time function which reasonably well explains the observed P

wave seismogram, and for the factor T_r/\bar{Q} (in equation (6)) of 2.0 and 3.0 sec. Figure 14 shows an example of the comparison between the synthetic P wave seismograms thus computed and the observed pP wave seismogram. Although the effect of the attenuation is to wide the entire pulse, the duration of the first half-cycle of pP wave is still longer than that of the synthetic P waves, even if the factor T_r/\bar{Q} appropriate for pP wave is given. This indicates that the difference between the pulse widths of P and pP waves is not only due to the difference of the ray paths but also due to the nonsymmetry of the pulse widths of P waves radiated from the focus. The nonsymmetry of the pulse widths indicates the Doppler-type effect associated with rupture propagation (see Fig. 5). The observed nonsymmetry of the pulse widths clearly indicates the downward propagation of rupture. This rupture mode is consistent with that estimated from the aftershock distribution relative to the main shock (Fig. 12).

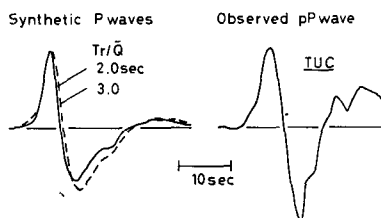


Fig. 14 Comparison of the observed seismogram of pP wave with the synthetic seismograms of P waves computed for the factor T_r/\bar{Q} of 2.0 and 3.0.

The nonsymmetry of the pulse widths of P waves is not apparent for the seismograms of the 1972 event because the signal of the foreshock contaminates that of the main shock (see Fig. 13 (b)). We must isolate the signal of the main shock from such seismograms. In the frequency domain, it is difficult to isolate the information of the main shock from the spectrum of such seismograms. The isolation can be done by the deconvolution technique in the time domain. This is of great advantage to the deconvolution technique as mentioned in section 2.1.

The P wave source time functions for each event were obtained from the WWSSN long-period seismograms by the deconvolution technique (Fig. 15). These source time functions were equalized back to a distance $r=1$ km from the focus. The stations together with other pertinent data used here are listed in Table 3. The isolation of the main shock pulse from the foreshock

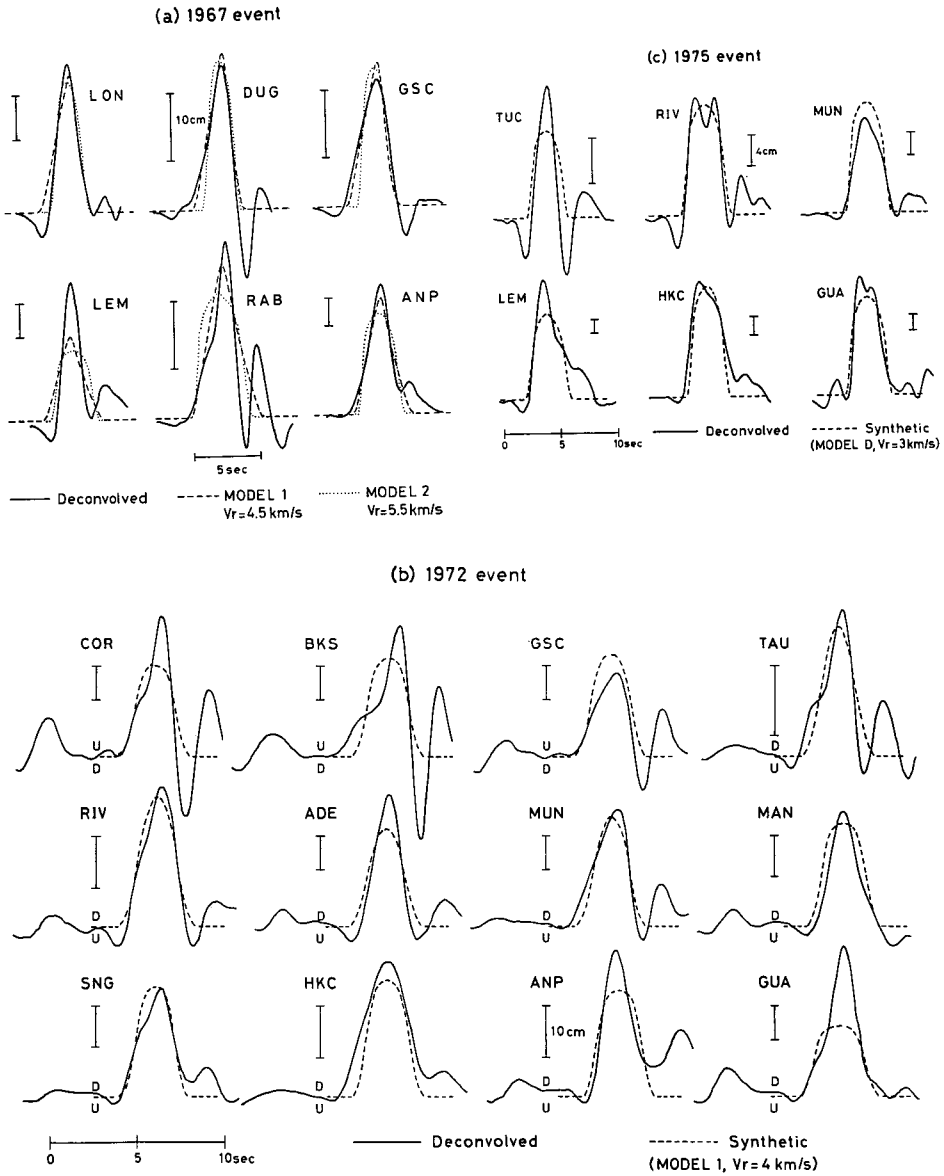


Fig. 15 Deconvolved source time functions of P waves and theoretical ones calculated for the most probable source parameters.

Table 3 Station data and seismic moment. Δ is the epicentral distance, Az the epicenter-to-station azimuth, and M_0 the seismic moment.

(a) 1967 event

Station Code	Δ deg.	Az deg.	M_0 , 10^{26} dyne-cm	Waves used
ADE	39	240	—	S
LEM	72	270	6.10	P
DUG	87	45	5.61	P
HKC	78	300	—	S
LON	85	36	5.69	P
MUN	58	245	—	S
NHA	78	288	—	pP
GSC	81	47	6.33	P
RAB	33	297	4.51	P, pP
PEL	93	127	—	pP
SPA	69	180	—	S
ANP	74	306	5.81	P, S
TUC	84	52	—	pP

Av. 5.68

(b) 1972 event

Station Code	Δ deg.	Az deg.	M_0 , 10^{26} dyne-cm	Waves used
ADE	36	245	3.66	P
BKS	84	43	3.73	P
COR	87	37	3.70	P
GUA	52	315	5.22	P
HKC	79	301	5.06	P, S
KIP	52	27	—	S
MAN	70	298	2.94	P
SNG	83	281	3.54	P
MUN	55	248	4.13	P, S
GSC	85	47	2.66	P
RIV	26	245	3.44	P
ANP	76	307	3.22	P, S
TAU	31	229	3.50	P

Av. 3.73

pulse for the 1972 event is accomplished well (Fig. 15(b)). Each source time function is characterized by a uni-directional, single pulse, except for those at stations COR and BKS for the 1972 event. The source time functions at stations COR and BKS show a return motion, the backswing of the source time function (Kikuchi and Fukao⁷³). However, such source time functions probably result from the incorrect choice of the base line as noted by Strelitz⁷⁴).

Table 3 Continued. (c) 1975 event

Station Code	Δ deg.	Az deg.	M_0 , 10^{26} dyne-cm	Waves used
ADE	38	245	—	S
ALQ	91	52	—	pP
ANT	95	119	—	pP
LEM	72	271	2.64	P
GUA	52	313	2.08	P, S
HKC	80	300	2.42	P
KIP	50	26	—	S
MUN	57	247	1.63	P, pP, S
NNA	96	106	—	pP
RIV	28	244	1.89	P
TUC	86	52	1.77	P, pP

Av. 2.07

The time integration of the source time function gives the seismic moment M_0 according to equation (13). The seismic moment was estimated to be $5.7(\pm 0.57) \times 10^{26}$ dyne-cm, $3.7(\pm 0.73) \times 10^{26}$ dyne-cm and $2.1(\pm 0.36) \times 10^{26}$ dyne-cm for the 1967, 1972 and 1975 events, respectively (see Table 3). From the seismic moments, static source parameters such as the average dislocation and the stress drop can be estimated for each fault model using equations (15) and (16).

In order to obtain the most probable rupture velocity and fault model, theoretical P and pP waves were computed for the static source parameters estimated and various rupture velocities, and then they were compared with the observed ones. For the computation of the theoretical wave forms, we take that $V_p=10.3, 9.5$ and 8.7 km/sec; $V_s=5.7, 5.2$ and 4.8 km/sec; and $\rho=4.1, 3.8$ and 3.6 g/cm³ for the 1967, 1972 and 1975 events, respectively. As the factor T_r/\bar{Q} appropriate for pP waves, that appropriate for P waves of shallow earthquakes was used. Barazangi et al.⁷⁵⁾ showed the existence of extremely low Q zone beneath Lau basin behind the Tonga arc. However, pP waves from deep-focus earthquakes ($h>300$ km) do not travel through this zone since this zone seems to exist in the upper 300 km of the mantle (see Fig. 1 in their paper).

Theoretical P wave source time functions were high-cut filtered and then they were compared with the deconvolved ones. For pP waves, the comparison between the synthetic and observed seismograms was made mainly on the pulse width, the peak amplitude of the synthetic seismogram being normalized to that of the observed seismogram. For the comparison, the

parameters R_f and R_g defined by equations (11) and (12) were used. The rupture velocity as well as the preferable fault model were determined so as to make R_f and R_g minimum.

Figures 16 and 17 show the variation of R_f and R_g for each fault model as a function of rupture velocities. For the 1967 event, the minimum values of R_f and R_g for Model 1 are much less than those for Model 2. Furthermore the

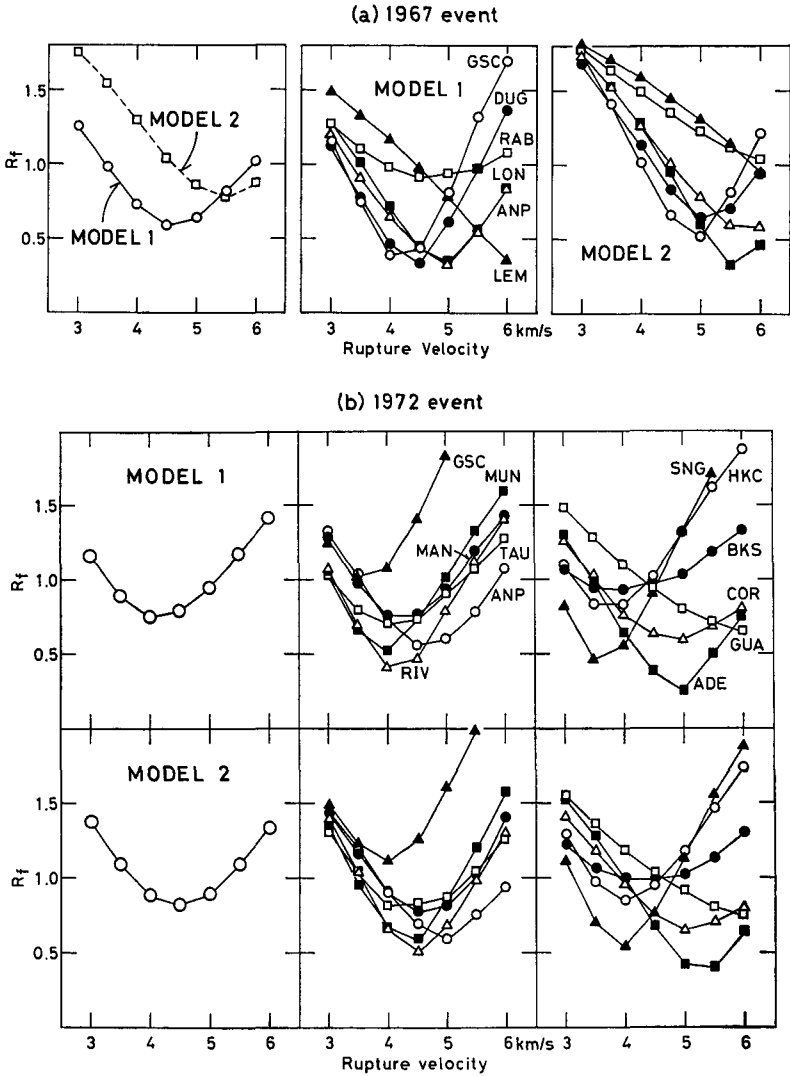


Fig. 16

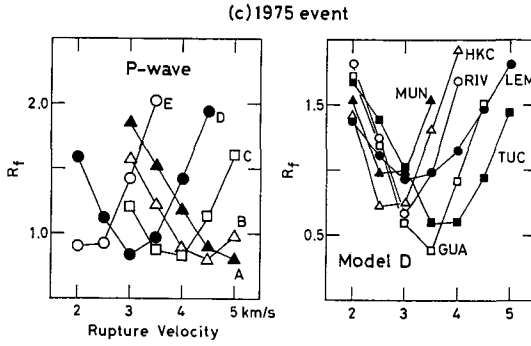


Fig. 16 Variation of parameter R_f for various rupture velocities and fault models.

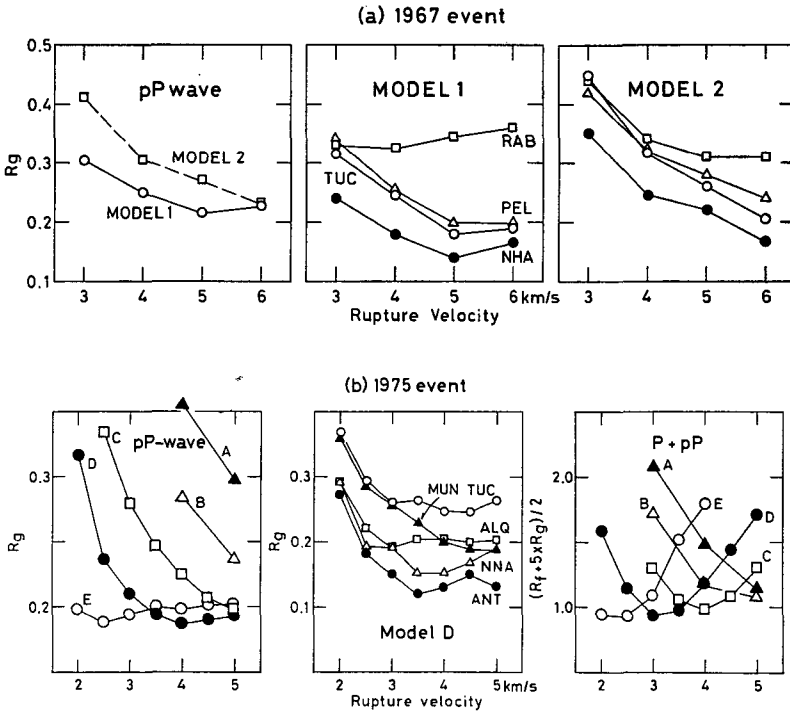


Fig. 17 Variation of parameter R_g for various rupture velocities and fault models. For the 1975 event, variation of parameter $(R_f + 5 \times R_g) / 2$ for various rupture velocities and fault models is also shown.

rupture velocity for Model 1 at the minimum of R_f is nearly the same as that at the minimum of R_g . These evidences imply that the most probable rupture velocity and fault model are 4.5–5.0 km/sec and Model 1 for the 1967 event, and that the estimation of the fault model from the spatial distribution of the aftershocks is reasonable for this event.

Model 1 and Model 2 for the 1972 event give approximately the same minimum value of R_f for the rupture velocity of 4.0 to 4.5 km/sec. Therefore, it is impossible to decide which of the fault models is more probable. Unfortunately, no analysis of pP wave seismograms was done for this event, because the pP wave signal of the foreshock contaminates that of the main shock as can be seen in Fig. 13(b).

For the 1975 event, it was assumed at first that the distance from the main shock to the aftershock is twice the major semi-axis a of the elliptical fault, that is, $2a=50$ km (see Fig. 12(c)). This assumption may be required by the dislocation theory as discussed earlier. However, for this fault model we could not obtain the rupture velocity, for which theoretical wave forms simultaneously explain the deconvolved source time functions of P waves and the observed seismograms of pP waves; the source dimension is too large to explain the observed seismic body waves. Then, by reducing the source dimension, we searched the most probable fault model and rupture velocity.

Five fault models were assumed for the 1975 event as follows: Model A, B, C, D and E (Table 4). For these fault models a/b was taken as 2. The average dislocation was varied depending on the fault model using equation (15). Figures 16(c) and 17(b) show the variation of R_f and R_g for these fault models against rupture velocities. The minimum values in R_f for these fault models are almost the same, while the minimums in R_g are different from one another. We calculated the quantities of $(R_f+5\times R_g)/2$ to obtain the most optimum rupture velocity as well as the reasonable fault model readily.

Table 4 Models and fault parameters for the 1975 event.

Fault parameter	MODEL				
	A	B	C	D	E
$2a$, km	30	25	20	15	10
$2b$, km	15	12.5	10	7.5	5
\bar{D} , m	0.7	1.0	1.6	2.8	6.3

a =major semi-axis of the elliptical fault;

b =minor semi-axis of the elliptical fault;

\bar{D} =average dislocation.

Since the magnitude of R_g is about one-fifth of that of R_f , the values of R_g are multiplied by 5.0 to uniform the values of R_g and R_f . The variation of $(R_f + 5 \times R_g)/2$ is shown on the right hand in Fig. 17(b). Model D and Model E among the five fault models have the lower minimum of $(R_f + 5 \times R_g)/2$ for the rupture velocities of 3.0 km/sec and 2.5 km/sec, respectively. Therefore these fault models and rupture velocities may be taken as the most probable ones.

For the elliptical fault model assumed, the P wave pulse width T_p is approximately related to the source parameters as $T_p \approx 2a/V_r - 2a \cos \theta / V_p$, where θ is the angle between the ray path and the rupture direction. If the source dimension is small, say $2a \approx 10$ km, then $2a/V_p$ (8.7 km/sec) $\lesssim 1.0$ sec, and T_p hardly varies depending on $\cos \theta$. T_p depends on the term $2a/V_r$ mainly. Therefore if an appropriate rupture velocity is selected, the fault model whose source dimension is smaller than that of Model E may be acceptable. However, if the earthquake that occurred at a distance of 50 km from the main shock is taken as the aftershock which was generated by the stress concentration due to the main shock fault, such a small source dimension is not acceptable for the main shock. This is because the stress concentration must rapidly fall off with distance from the main shock fault (Rybicki⁽⁶⁸⁾). Based on above discussions, Model D with $V_r = 3$ km/sec was taken as the most probable fault model, but this may be the upper limit for the source area. The longer size of this fault model is about one-third of the distance between the foci of the main shock and aftershock.

Figure 15 shows the comparison of the deconvolved source time functions of P waves with the theoretical ones computed for the most probable source parameters obtained. Figure 18 shows the comparison of the observed seismograms of pP waves with the theoretical ones computed for the most probable source parameters obtained. A good agreement between the deconvolved and theoretical source time functions as well as between the observed and theoretical pP wave seismograms is obtained. The sensitivity of the parameters R_f and R_g to the change in the wave form can be seen by comparing Fig. 15(a) with Fig. 16(a) and Fig. 18(a) with Fig. 17(a), respectively.

Analysis of S waves

The analysis of S wave seismograms is to confirm the source parameters obtained from analyses of P and pP waves. Synthetic seismograms of S waves were computed by convolution of S wave source time function with the impulse response of the transmitting system, on the assumption that the

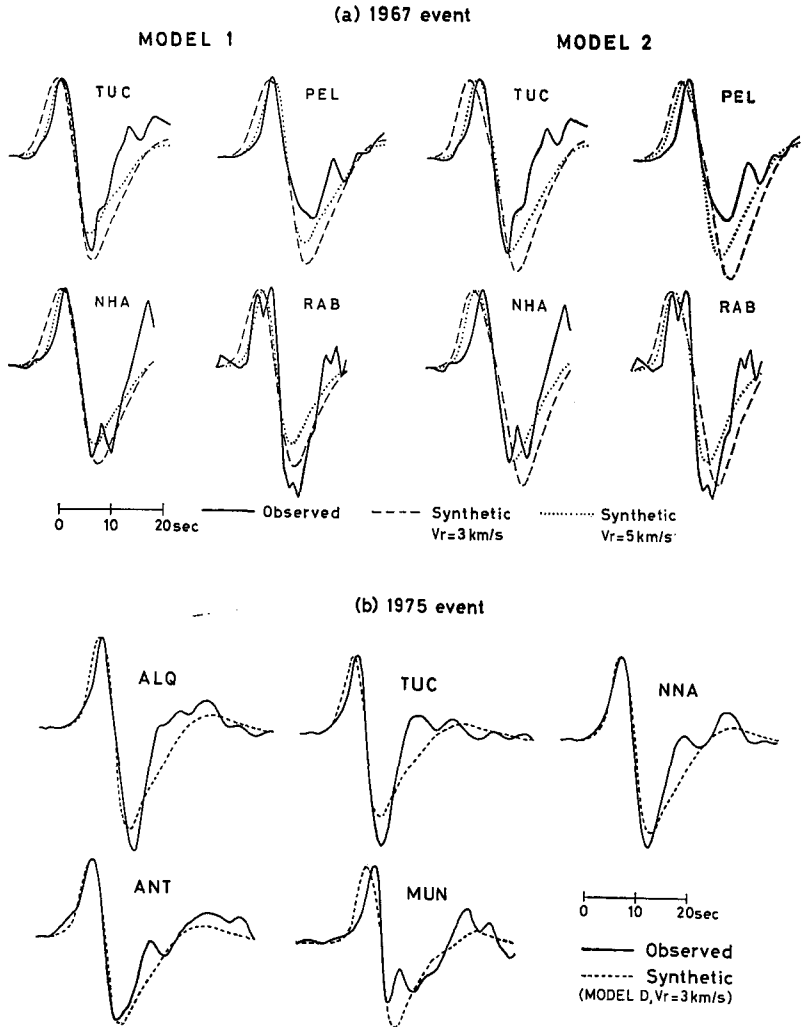


Fig. 18 Observed seismograms of pP waves and synthetic ones calculated for the most probable source parameters. Amplitude is normalized.

specific quality factor for S wave is a half that for P wave at all depths. Seismograms of SV- and SH-waves were computed at first and then they were decomposed into NS- and EW-components by the rotation of axis to compare the synthetic seismograms directly with the observed seismograms.

Figure 19 shows the observed seismograms and the synthetic seismograms

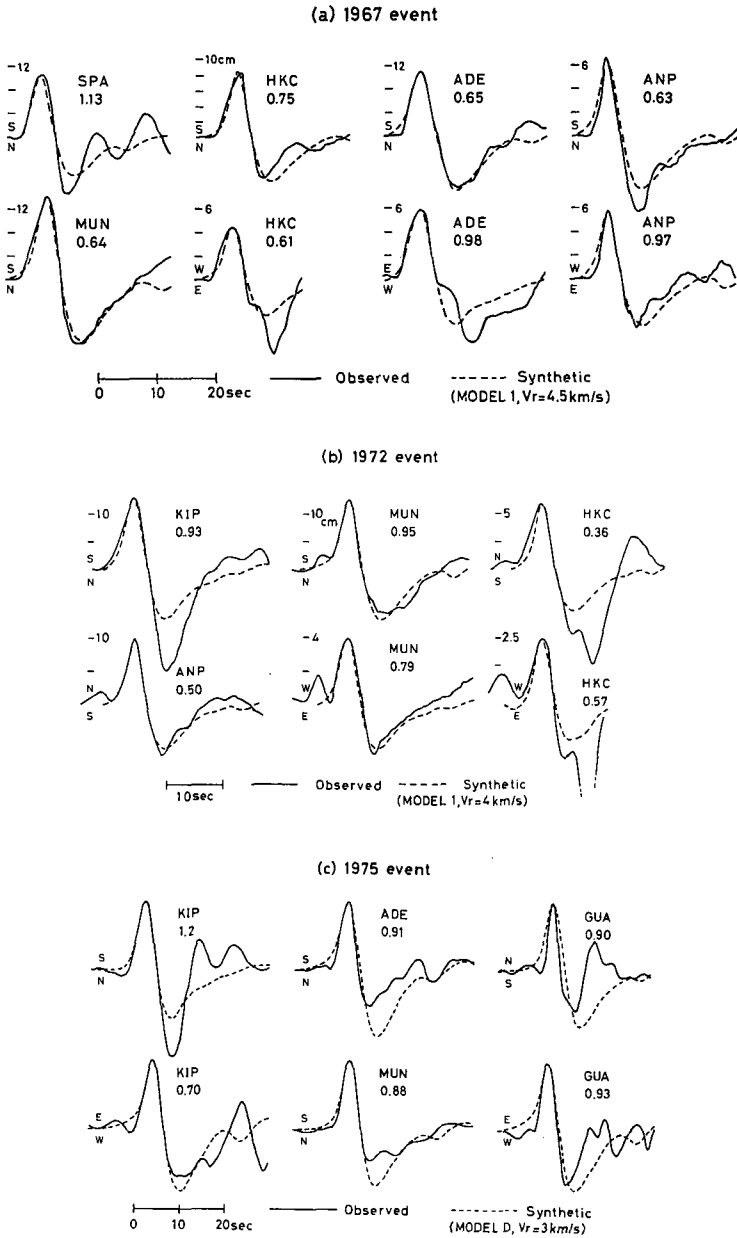


Fig. 19 Observed seismograms of S waves and synthetic ones calculated for the most probable source parameters. Amplitude is normalized. The numbers attached to each station code indicate the amplitude ratio of the observed seismogram to the synthetic seismogram.

computed for the most probable source parameters for each event. In the present study it is attempted to compare only the first half-cycle. Synthetic wave forms explain reasonably the observed wave forms of at least the first half-cycle. This confirms that the results obtained from the analyses of P and pP waves are reasonable. The discrepancy in the waves after the first pulse arrival is probably due to a minor difference between the crustal structure used in the calculation and that beneath the observation point or due to a later phase such as ScS wave or due to both.

2.3 An intermediate-depth earthquake near Tomakomai in Hokkaido, Japan Aftershocks and focal mechanism solution

This earthquake occurring on Nov. 8, 1974 was accompanied by three aftershocks ($M \sim 3.0$). The hypocenters of the main shock and three aftershocks were determined with high accuracy from the P times observed at four volcanological stations of JMA and five microearthquake stations of Hokkaido University (Fig. 20 and Table 5). The aftershocks occur in a region shallower than the main shock. The area in which these hypocenters were determined is elongated in the northeast-southwest direction.

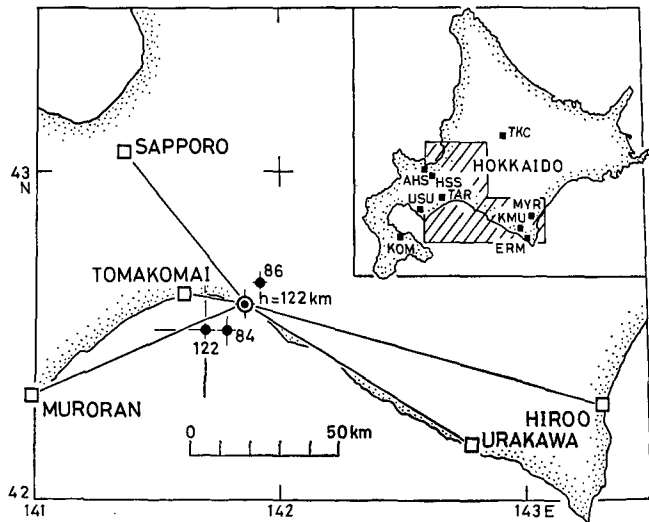


Fig. 20. Spatial distribution of the aftershocks of the intermediate-depth earthquake near Tomakomai. The inset shows stations used in determination of the hypocenters. The numbers attached to each epicenter indicate the focal depth.

Table 5. Focal coordinates of the main shock and the aftershocks of the intermediate-depth earthquake near Tomakomai.

No.	Date m d y	Origin time h m s	Lat. . °N	Long. °E	Depth km	m_b	RMS sec
1	Nov. 08, 1974	21 23 23.0	42.60	141.86	122	6.0	0.415
2	Nov. 08, 1974	22 23 45.2	42.52	141.70	122	—	0.723
3	Nov. 09, 1974	03 57 05.0	42.67	141.92	86	2.9*	0.406
4	Nov. 12, 1974	17 47 34.2	42.52	141.79	84	2.8*	0.507

* after Bulletin of the Urakawa Seismological Observatory and the Sapporo Seismological Observatory.

Figure 21 shows the focal mechanism solution for the main shock determined on the basis of the first motions of P and pP waves together with the polarization angles of S waves. The standard deviation of the S wave polarization angles is 19.1° . For the solution the first motions of P waves reported in the seismological bulletin of JMA were also used. The aftershocks occur near the steeply dipping nodal plane striking in the northeast-southwest direction. Referring to the relation of aftershocks and the mechanism solution of the main shock described in the preceding section, this nodal plane is taken as the actual fault plane. In addition, the rupture is inferred to propagate upward on this plane. Based on the aftershock distribution, a rectangular fault model may be assumed as shown in Fig. 22, in which the

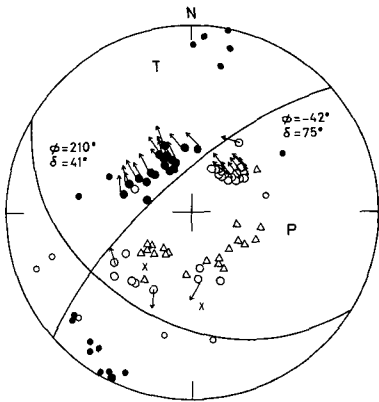


Fig. 21 Focal mechanism solution for the main shock. Symbols are the same as in Fig. 10.

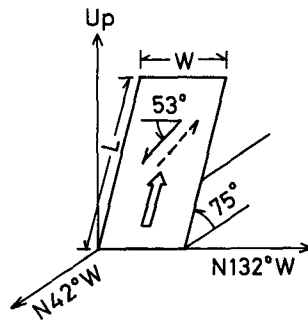


Fig. 22 Geometry of the fault model assumed. A hollow arrow indicates the direction of rupture propagation.

dislocation takes place simultaneously over the fault width W and propagates at a constant velocity along the fault length L .

Analysis of S waves

Figure 23(a) shows near-field seismograms recorded by the strong motion seismograph of JMA. P wave signals are very weak but S wave signals are predominant. Figures 23(b) and 23(c) show far-field S and P wave seismograms recorded by the WWSSN long-period seismograph. S wave signals of the seismograms are also predominant. Therefore, in the analysis, both S waves which are direct waves radiated upward and downward from the focus can be used. The pulse width of P waves seems to be slightly longer than that of pP waves as can be seen in Fig. 23(c). This is not the case for the Tonga earthquakes (see Fig. 13). The difference of the pulse widths of these waves indicates that the rupture propagated upward as inferred from the aftershock distribution. For P and pP waves no detailed waveform analyses were made because of weak signals of the waves.

In order to determine the source parameters, synthetic seismograms of S waves were computed for the assumed fault model and they were compared with the observed seismograms. In computing the dynamic near-field displacement to be required, Haskell's method⁵³⁾ described in section 2.1 was used. A free-surface effect is included simply by doubling the amplitude calculated for an infinite medium. Synthetic seismograms in the far-field were computed by substituting equation (8) into equations (10) and (1). Velocities of P and S waves and density for the computation are given as 8.0 km/sec, 4.5 km/sec and 3.4 g/cm³, respectively. The S wave analysis was made in detail for the EW-component seismograms at Tomakomai and Sapporo in the near-field and at station KEV in the far-field, where clear signals were recorded.

Although the epicentral distance is small for the stations in the near-field ($d < 70$ km), S wave displacements at these stations are almost similar to that at station KEV in the far-field because of a large focal depth (Fig. 24). The pulse width of the displacement or the source time function, T_s (see Fig. 24), is a main factor to change the wave form of S wave seismograms; the duration of the first half-cycle of the waves is changed with T_s (Bollinger²³⁾; Sasatani⁷²⁾). T_s is suitably obtained so that the synthetic seismograms may fit the observed ones. The values of T_s obtained are 2.5–3.0 sec, 2.0–2.5 sec and 7.5–8.5 sec for the seimograms at stations Tomakomai, Sapporo and KEV,

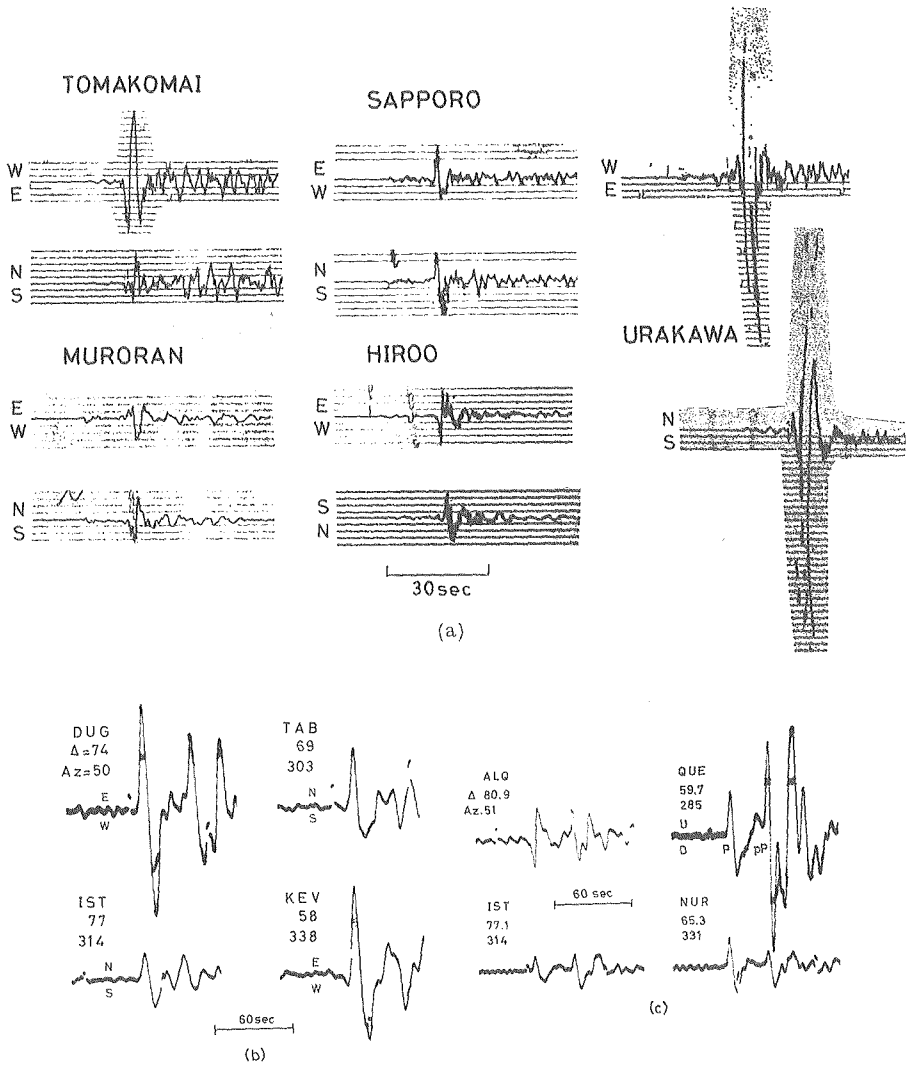


Fig. 23 (a) Near-field seismograms of the intermediate-depth earthquake near Tomakomai, recorded at Tomakomai, Sapporo, Murooran, Urakawa and Hiroo. (b) Far-field seismograms of S waves (WWSSN long-period seismograms). (c) Far-field seismograms of P and pP waves (WWSSN long-period seismograms).

respectively. These values of T_s clearly indicate that the rupture propagated upward (the Doppler-type effect). T_s is approximately related to the source parameters through the equation as

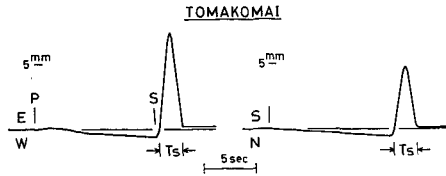


Fig. 24 Ground displacements at Tomakomai calculated for Model A (see Table 6). T_s indicates the pulse width of S wave.

$$T_s \approx \frac{L}{V_r} - \frac{L}{V_s} \cos \theta + \tau$$

where θ is the angle between the ray path and the rupture direction. Source parameters such as L , V_r and τ must be selected so as to satisfy the above equation.

Based on the aftershock distribution, a fault model with $L=40$ km and $W=20$ km may be assumed. Substitution of the observed values of L and T_s into above equation, however, shows that this fault model does not provide reasonable values of V_r and τ . The unreasonable values of V_r and τ are due to the source dimension which is estimated to be unreasonably large. To obtain the most probable fault model together with the reasonable values of V_r and τ , tentative calculations of the above equation were made for various combinations of fault lengths (10, 15, 20, 30 km), rise times (0.5, 1.0, 1.5, 2.0 sec) and rupture velocities (2.0, 3.0, 3.5, 4.0 km/sec). A few combinations of these source parameters, however, can be rejected as unreal case. The comparison between the observed and synthetic seismograms was made for six fault models whose source parameters are shown in Table 6. For the fault models, it is assumed that $L/W=2$, which is safely applied to fault models of many shallow earthquakes (Kanamori and Anderson⁶⁹; Abe⁷⁰; Geller⁷¹). The

Table 6 Model and fault parameters.

Fault parameter	MODEL					
	A	B	C	D	E	F
L , km	15.0	15.0	20.0	15.0	15.0	15.0
W , km	7.5	7.5	10.0	7.5	7.5	7.5
V_r , km/s	3.5	3.5	3.5	4.0	4.0	3.0
τ , sec	1.0	2.0	1.0	0.5	1.5	0.5

L =fault length; W =fault width; V_r =rupture velocity; τ =rise time.

selection of the most reasonable model was made on the magnitude in parameter R_g of equation (12).

Figure 25 shows the variation of R_g for six fault models. Models A and E among these models give the minimum R_g . Source parameters for the models are: $L=15$ km, $W=7.5$ km, $V_r=3.5-4.0$ km/sec and $\tau=1.0-1.5$ sec. Figure 26 shows the observed seismograms and the synthetic seismograms for Models A, C and D. Figure 27 shows the comparison of the observed far-field seismograms of S waves with the synthetic seismograms for Model A. As far as the duration of the first half-cycle is considered, the agreement between these seismograms is good not only at station KEV but also at the other stations.

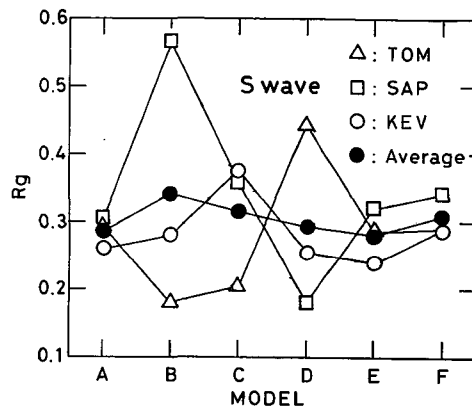


Fig. 25 Variation of parameter R_g for various fault models in Table 6.

The synthetic S wave seismograms for Model A at stations Hiroo and Muroran satisfactorily fit the observed seismograms as shown in Fig. 28. The observed seismograms of S waves at Urakawa are off scale (see Fig. 23(a)). Such a large amplitude of the seismograms cannot be explained by Model A. This is an unsolved problem.

From comparison of amplitudes between the observed seismograms and the synthetic ones for Model A at four near-field stations, the average dislocation was estimated to be 82.6 cm (Table 7). Using this value of \bar{D} , $S=15 \times 7.5$ km² and $\mu=0.69 \times 10^{12}$ dyne/cm², we had $M_0=6.41 \times 10^{25}$ dyne-cm. The comparison of amplitudes between the observed seismograms and synthetic ones for Model A at nine stations in the far-field gives a total seismic moment of 6.25×10^{25} dyne-cm (Table 8). From equation (15) the average dislocation

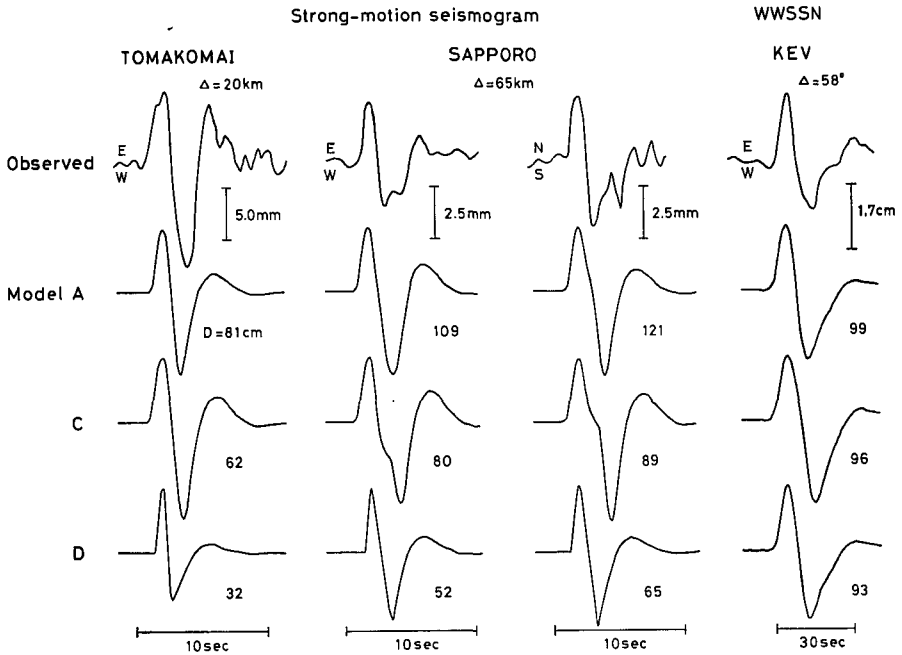


Fig. 26 Observed seismograms of S waves and synthetic ones calculated for Models A, C and D. The numbers attached to each synthetic seismogram indicate the average dislocation.

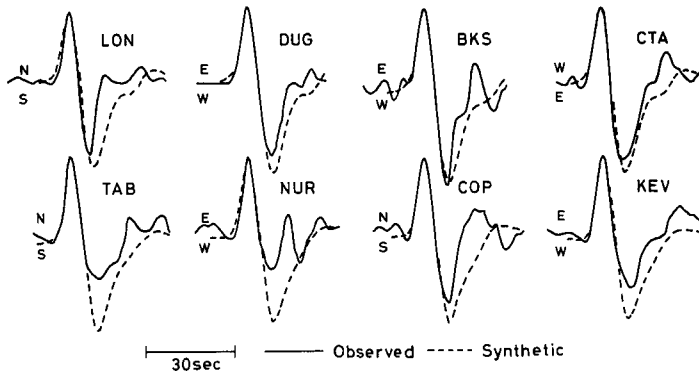


Fig. 27 Observed far-field seismograms of S waves and synthetic ones calculated for Model A. Amplitude is normalized.

was estimated to be 80.5 cm. On the average of these obtained values we had $M_0=6.3 \times 10^{25}$ dyne-cm and $\bar{D}=82$ cm. Using these values the stress drop was estimated to be about 130 bars.

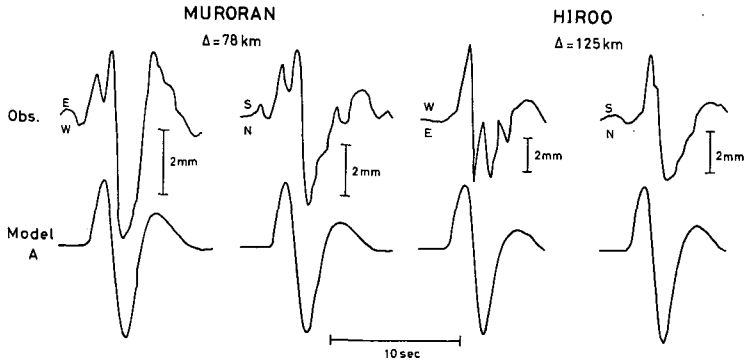


Fig. 28 Observed seismograms of S waves and synthetic ones calculated for Model A.

Table 7 Near-field station data and average dislocation.

Station	Δ km	Az deg.	Average dislocation	
			N-S comp.	E-W comp.
Tomakomai	20	280	40.5	80.9
Sapporo	65	322	121.0	108.7
Muroran	78	246	53.4	77.5
Hiroo	125	106	96.2	—

Av. 82.6 cm

Table 8 Far-field station data and seismic moment.

Station Code	Δ deg.	Az deg.	$M_0 \times 10^{25}$ dyne-cm	
			N-S comp.	E-W comp.
BKS	70	57	6.3	5.3
COL	44	35	7.4	—
COP	73	333	5.5	—
CTA	62	175	2.8	1.8
DUG	74	50	5.5	5.9
KEV	58	338	11.0	7.8
LON	64	49	4.7	7.9
NUR	65	331	7.6	8.7
TAB	69	303	6.3	5.5

Av. 6.25

2.4 Discussion

In this section we shall summarize the source parameters of deep-focus earthquakes obtained in the preceding sections and those reported by other

Table 9 Source parameters

No.	Date	Region	Epicenter	
			Lat.	Long.
1	Oct. 09, 1967	West of Tonga	21. 14° S	179. 16° W
2	Aug. 30, 1970	Sea of Okhotsk	52. 36° N	151. 64° E
3	Jan. 29, 1971	Sea of Okhotsk	51. 69° N	150. 97° E
4	Mar. 30, 1972	South of Fiji	25. 77° S	179. 61° E
5	Nov. 08, 1974	near Tomakomai	42. 60° N	141. 86° E
6	Feb. 22, 1975	South of Fiji	24. 97° S	178. 88° W

M_0 =seismic moment; S =source area; \bar{D} =average dislocation;

authors. Further, we shall discuss about the physical properties of the focal region. The source parameters obtained in the present study are given in Table 9, in which the source parameters of two deep-focus earthquakes of the Sea of Okhotsk obtained in the previous papers (Sasatani^{36),37)} are also included.

Accuracy of determination of source parameters

Among source parameters, the total seismic moment, the accuracy of which is better than about 20%, can be considered as the most reliable one to understand the static properties of the earthquake source, since this parameter is independent not only of the rupture velocity but also of the rupture geometry. The source area was estimated from both the spatial distribution of the aftershocks and the wave-form analysis of seismic body waves radiated in the various directions. Therefore, the source area was estimated in the accuracy better than a factor 1.5. The accurate determination of the source area improved the accuracy of determination of the other source parameters. The rupture velocity was estimated in the accuracy of ± 0.5 km/sec. Since the average dislocation and stress drop were computed using the determined seismic moment and source area (equations (15) and (16)), these parameters were estimated within a factor 2. The accurate estimation of the rise time of slip dislocation is difficult, then the source parameters of three Tonga deep-focus earthquakes were determined on the assumption that the dislocation occurred stepwise, that is, $\tau \approx 0$ sec. For one intermediate-depth earthquake, we obtained $\tau = 1.0$ – 1.5 sec. If $\tau \leq 1.0$ sec, no correction of the source parameters is required for the Tonga earthquakes.

The fault geometry assumed through the analyses (rectangle, ellipse and triangle) is not essential, because the number of the aftershocks is not so

of deep-focus earthquakes.

Depth km	m_b	M_0 $\times 10^{26}$	S km ²	\bar{D} m	$\Delta\sigma$ bar	V_r km/sec
607	6.2	5.7	110	4.0	1200	4.5-5.0
643	6.5	11.0	420	1.9	320	4.0
515	6.0	2.8	200	1.2	240	4.5
485	6.1	3.7	160	2.3	460	4.0-4.5
122	6.0	0.6	110	0.8	130	3.5-4.0
338	6.1	2.1	88	2.8	610	3.0-3.5

$\Delta\sigma$ =stress drop; V_r =rupture velocity.

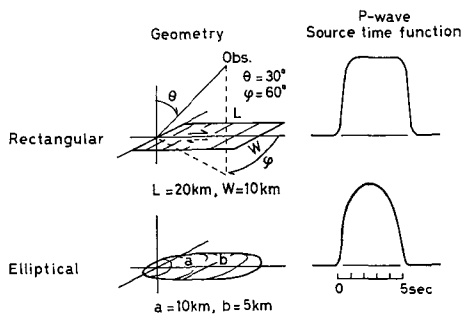


Fig. 29 Changes of the P wave source time functions due to changes in fault geometry.

many to determine the detailed fault geometry. Considering the quality of the data used in the analyses, it is also difficult to obtain the detailed fault geometry through the analysis of the deconvolved source time functions; as shown in Fig. 29, both source time functions from the rectangular fault model and the elliptical fault model are nearly the same. In fact, both rectangular and elliptical fault models for the south of Fiji earthquake of 1972 give similar results as shown in section 2.2. The point emphasized is the inference that the rupture propagates uni-laterally along the steeply dipping nodal plane and almost covers the source area determined.

Aftershocks and source process of the main shock

The aftershocks presented in sections 2.2 and 2.3 were located near one of two nodal planes of the mechanism solution of the main shock. Taking this nodal plane as a fault plane and assuming the rupture mode on the basis of the relative hypocenter locations of the main shock and aftershocks, the

observed P, pP and S waves can be explained reasonably by the synthetic waves. This clearly shows that a kinematic source model for deep-focus earthquakes is a shear faulting.

The nodal plane selected as the fault plane is the steeply dipping plane for all earthquakes studied. Oike⁷⁶⁾ found that aftershocks for most deep-focus earthquakes were located near the steeply dipping nodal plane of the main shock and he assumed that this plane may be taken as the fault plane. Although his assumption has not been investigated in the analysis applied to seismic waves, our result supports his assumption. These evidences suggest that the steeply dipping nodal plane rather than the gently dipping nodal plane is likely to form the actual fault plane, and support the Fukao's idea⁷⁷⁾ that the faulting must do some work against gravity along the steeply dipping plane in the gravitationally sinking lithosphere. On the other hand, Savage⁷⁸⁾ and Ritsema⁷⁹⁾ considered that the slip displacements during deep-focus earthquakes occurred almost in the horizontal fault plane. The present results, however, are incompatible with their consideration.

The aftershocks of the 1967 and 1972 Tonga events approximately outline the source area of the main shock. On the other hand, the aftershocks of the 1975 Tonga event and the intermediate-depth earthquake near Tomakomai occurred at a region considerably apart from the source area of the main shock. These evidences suggest the existence of two types in occurrence of aftershocks as follows: TYPE 1A, aftershocks occurring at the region very close to the fault of the main shock; and TYPE 1B, aftershocks occurring at the region considerably apart from the fault of the main shock. Although it has been considered that the spatial distribution of aftershocks outlines the source dimension of the main shock, the occurrence of aftershocks of TYPE 1B shows that this consideration is not necessarily true. Two types of occurrence of aftershocks will be discussed in detail in chapter 3.

Source area and stress drop

Figure 30 shows source areas plotted against total seismic moments. The results obtained by Mikumo²⁷⁾, Fukao³⁰⁾, Koyama³⁴⁾ and Abe¹⁸⁾ are also shown in the figure. These were obtained from analysis of seismic waves in the time domain as is used in the present study. For shallow earthquakes, the intra-plate earthquakes which occur within the plate, the source area and total seismic moment are shown for comparison. These were taken from Table 1 in the paper of Kanamori and Anderson⁶⁹⁾. Although the source area of both

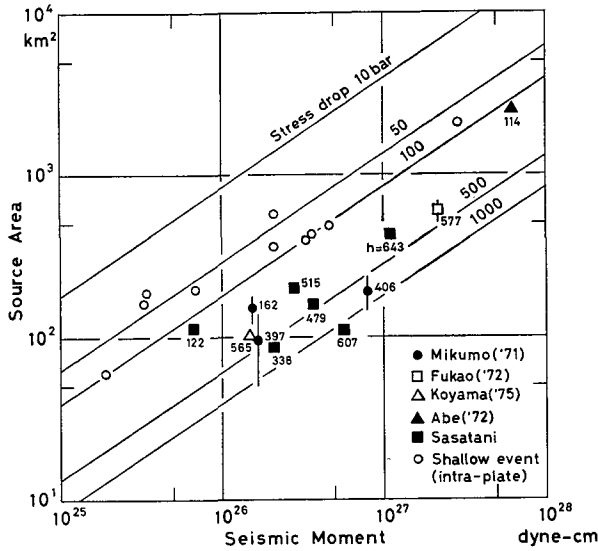


Fig. 30 Relation between source area and seismic moment. The straight lines give the relations for circular cracks with constant stress drop. The numbers attached to each deep-focus earthquake indicate the focal depth.

shallow and deep-focus earthquakes increases with total seismic moment, the source area of deep-focus earthquakes is much smaller than that of shallow earthquakes for a given seismic moment.

Source dimension of a deep-focus earthquake is 20 to 30 km at most. The large deep-focus earthquake has been interpreted as an earthquake that is not caused by a single large fault but caused by a multiple shock composed of several earthquakes with a source dimension of 20 to 30 km (Fukao³⁰); Sasatani³⁷); Chung and Kanamori⁴⁴); Furumoto⁸⁰). This source dimension suggests that for deep-focus earthquakes the stress concentration at the focus is quite limited in a region. The region is included in the lithosphere the thickness of which has been estimated to be about seventy kilometers (Kanamori and Press⁸¹); Yoshii⁸²), and has an effective (elastic) thickness of 20 to 30 km. The material in the region is responsible for the generation of deep-focus earthquakes. The effective thickness of the lithosphere may be consistent with that on the seaward side of deep-sea trenches obtained by Hanks⁸³) and Watts and Talwani⁸⁴).

The source area and total seismic moment are related to the stress drop through equation (16). The straight lines in Fig. 30 are to show the relations

for circular cracks with constant stress drop. These lines show that the stress drop is clearly larger for deep-focus earthquakes than for shallow earthquakes.

Figure 31 shows the obtained stress drops as a function of focal depths. Although the plots are somewhat scattered, it may be said that the stress drop increases with focal depths. The similar relation was derived also by Mikumo²⁷⁾. Our precise determination of the stress drops make the relation firmer. The average stress drop at a given depth range is 60 ± 30 bars for $0 < h < 50$ km (Abe⁷⁰⁾), 160 ± 45 bars for $100 < h < 200$ km and 520 ± 270 bars for $300 < h < 650$ km. The average stress drops in the depths will be used in chapter 3 to study the rupture mechanism of multiple shocks.

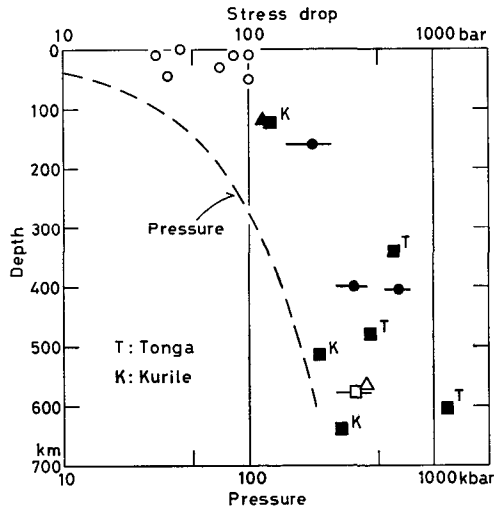


Fig. 31 Stress drops and hydrostatic pressure against focal depths. Symbols are the same as in Fig. 30.

Although the number of data is limited, the regionality of the stress drop is found; the stress drops in the Tonga arc are slightly larger than those in the Kurile arc. Deep seismicity in the Tonga arc is known to be quite active as compared with that in the Kurile arc (Sykes⁴⁾; Mizoue⁸⁵⁾). The stress drop may be closely related to the deep seismicity.

Wyss and Molnar³²⁾ obtained the stress drops for the Tonga deep-focus earthquakes with $m_b \approx 5.8$ from "corner frequency (corner period)" in the spectrum on the basis of the Brune's source model⁸⁶⁾. Their results are: the

stress drops are between 4 and 70 bars, the average of which is about 10 bars and the stress drops are hardly changed with depths, but appear to be slightly larger at intermediate depths than at great depths. The stress drops they obtained are smaller by about two order of magnitude than those obtained in the present study, and the relation between the stress drops and focal depths they obtained is different from that in Fig. 31. These differences may be partly due to the difference of earthquake magnitude and also partly due to the difference of the source models used. But it should be noted that the Brune's source model is so simple that the effect of the rupture propagation is not included, and that a small error in the corner frequency may produce a large error in the stress drop being proportional to the cube of the corner frequency. In addition, Linde et al.⁸⁷⁾ showed in their numerical study that the corner frequency obtained from a multiple shock, which occur very frequently in the deep seismic zone as shown in the following chapter, gives incorrect stress drop.

Rupture velocity

The source parameters of deep-focus earthquakes have been obtained on assuming a rupture velocity (Berckhemer and Jacob²²⁾; Mikumo²⁷⁾). A few authors (Chandra²⁸⁾; Oike⁴¹⁾) have regarded the apparent rupture velocity obtained from the multiple shock analysis (see chapter 3) as the true one. The apparent rupture velocity, however, cannot be taken as the true one for such multiple shock that the distance connecting hypocenters of the multiple shock exceeds the source dimension of the first shock (in detail see chapter 3). In the present study, determination of the source parameters has been done

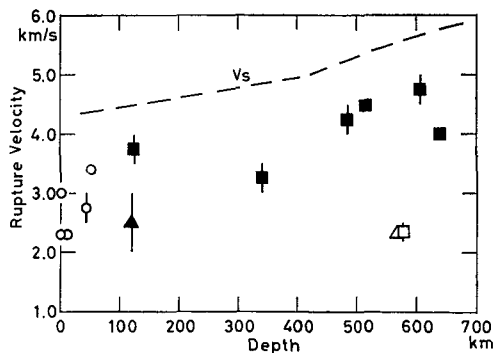


Fig. 32 Rupture velocities against focal depths. Symbols are the same as in Fig. 30.

without any assumption on the rupture velocity.

Figure 32 shows the rupture velocities as a function of focal depths. The rupture velocity at a depth is less than S wave velocity at the corresponding depth, that is, 70 to 80% of V_s . Such difference of the rupture velocity from S wave velocity is consistent with that expected from the mathematical considerations (Mansinha⁸⁸); Richards⁸⁹), and laboratory experiments (Wu et al.⁹⁰); Johnson and Scholtz⁹¹).

Fault movements during earthquakes and deformation of the lithosphere

Sasatani^{66,92}) found the intimate relation between the sense of fault movements during earthquakes and the sense of deformation of the descending lithosphere at the junction of the Kurile and Northern Honshu arcs. Here we examine the relation at the Tonga arc.

Figure 33(b) shows the vertical sections of earthquake hypocenters on profiles across the Tonga arc (Sykes⁴). The descending lithosphere is not simple configuration but is deformed as shown in Fig. 33(c). The sense of fault movements during earthquakes obtained in the present study is also shown in Fig. 33(c). This figure shows that the fault movements increase the deformation of the lithosphere.

Focal mechanism solutions of deep-focus earthquakes in the Tonga arc except the north region are similar to those obtained in the present study (Isacks et al.⁹³); Isacks and Molnar¹¹). This suggests that the predominant fault movement during deep-focus earthquakes in the Tonga arc is similar to those as shown in Fig. 33(c): the east side block moves downward relative to the west side block. These evidences indicate that the plastic deformation of the lithosphere may result from the fault movements associated with deep-focus earthquakes.

3. Rupture mechanism of deep multiple shocks

3.1 Complex seismograms

Data used in the analysis were taken from the WWSSN long-period seismograms. Seismograms from a single deep-focus earthquake show very simple wave form especially in the part of P waves; the wave form is similar to an impulse response of the seismograph as shown in Figs. 13, 23 and 34. For most deep-focus earthquakes, however, complicated wave form is frequently recorded in the portion of P wave; for example, the seismograms of

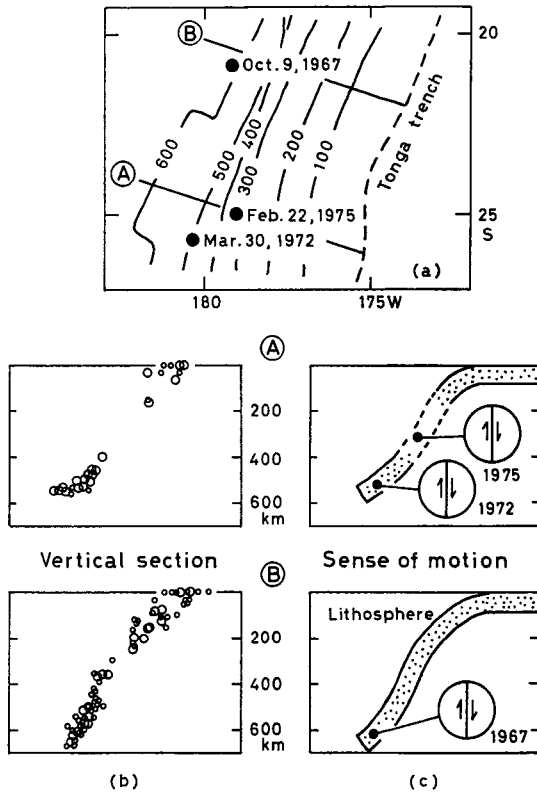


Fig. 33 (a) Map showing the iso-depth lines of deep-focus earthquakes in the Tonga arc (Isacks and Molnar¹¹), and the epicenters of earthquakes studied. (b) Vertical sections oriented perpendicular to the Tonga arc. Location of sections is shown in (a). (c) Schematic illustration of the descending lithosphere and the fault movements during earthquakes.

P wave arrival have such characteristics as waves show abrupt change in phase or sudden substantial increase in amplitude, and sometimes consist of sequence of some simple pulses. Among possibilities to complicate the wave form, crustal structure beneath stations, waves reflected from the surface of the earth (pP waves) as well as waves reflected from the core-mantle boundary (PcP waves), inhomogeneities in medium near the source, and source characteristics may be considered. As shown in Fig. 34, among seismograms of deep-focus earthquakes obtained at a given station, some ones show simple wave form, while other ones show complicated wave form. Further-

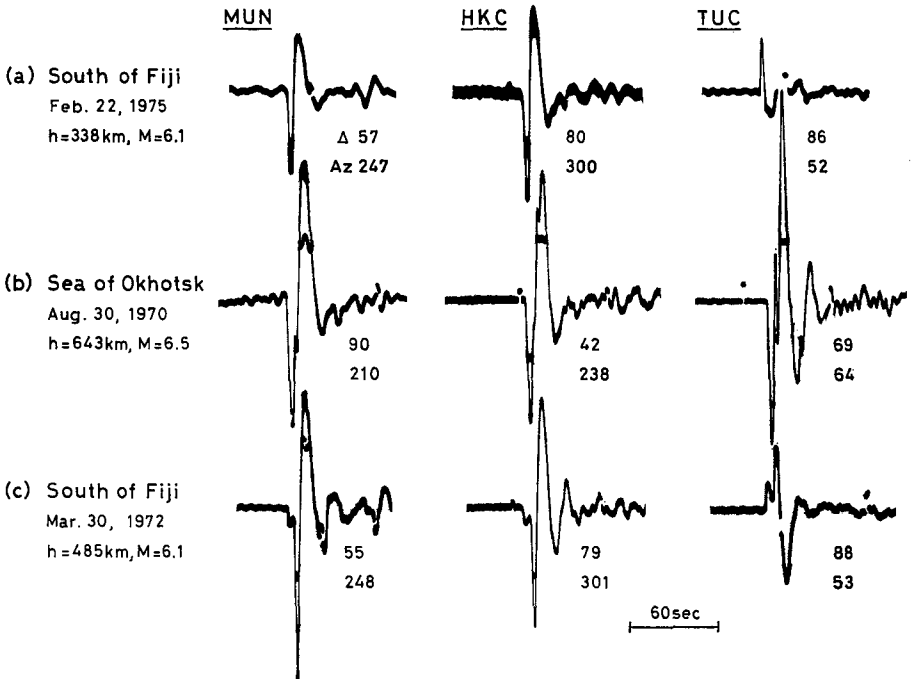


Fig. 34 WWSSN long-period seismograms (vertical component) of P waves for three deep-focus earthquakes, recorded at stations MUN, HKC and TUC. (a) a single event, (b) and (c) a multiple shock.

more, the wave form is different from earthquake to earthquake. Such different wave forms recorded at a station suggest that crustal structure beneath stations cannot be the cause to disturb the wave form.

Figure 35 shows travel time differences between the teleseismic direct P or S wave and other later phases such as pP, PcP, sP and sS waves for different focal depths. At focal depths greater than 100 km and at distances less than 75° , no arrivals are expected for about 10 sec after P phase. Therefore the complex wave form in P phase is not caused by such pP, PcP and sP phases. At distances beyond 80° PcP wave arrives less than 10 sec after direct P wave so that the PcP wave may disturb a portion of the direct P wave. However, even if such cases are excluded, the complicated waves have been recorded.

The inhomogeneity in medium near the source will hardly affects long-period waves when the size of the inhomogeneity does not exceed the wave

length of the wave; that is, the inhomogeneity also cannot be the cause of the wave form disturbance.

The disturbance of the waves, or the complicated wave is most likely caused by the earthquake source, at which the multiple shock is of highest possibility to disturb the wave form.

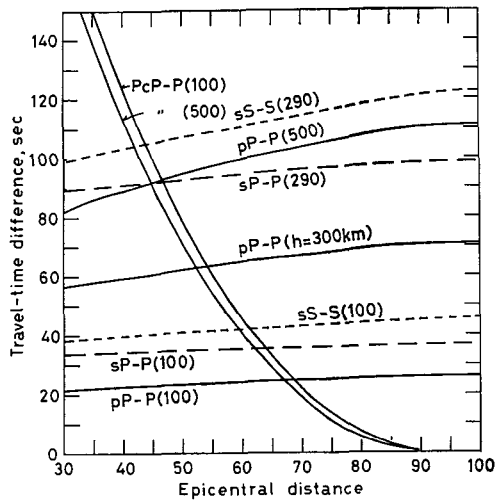


Fig. 35 Travel-time differences between the teleseismic direct P or S wave and major later phases for various focal depths (taken from Herrin⁹⁴⁾ for P waves, and from Jeffreys and Shimshoni⁹⁶⁾ for S waves).

Frequency of occurrence of deep multiple shocks

First we investigate the frequency of occurrence of deep multiple shocks. Sixty-four deep-focus earthquakes ($h \geq 100$ km) with a magnitude greater than about 5.9 which occurred throughout the world during the period from 1954 to 1978 were used in the investigation. Seismograms of these earthquakes at different stations were examined upon the wave form in order to discriminate whether the earthquake can be characterized with the multiple shock or not.

The earthquakes were classified in terms of source type (a single event or a multiple shock) and the results are shown by regional groups in Table 10. About fifty-four percent of intermediate-depth earthquakes ($100 \leq h < 300$ km) and about seventy-six percent of deep-focus earthquakes ($h \geq 300$ km) were identified with the multiple shock; the earthquakes deeper than about 300 km occur in the form of the multiple shock with very high probability. Con-

Table 10 Frequency of occurrence of deep multiple shocks.

No.	Region	Number of Events Studied		Number of Multiple Shocks	
		<i>I</i>	<i>D</i>	<i>I</i>	<i>D</i>
1	Solomon-New Britain-New-Guinea	4	1	3	1
2	New Hebrides	9	0	4	0
3	Tonga	1	5	0	3
4	Kermadec-New Zealand	3	0	1	0
5	Peru-Chile	2	5	1	4
6	Colombia, South America	2	1	2	1
7	Aleutians	1	0	1	0
8	Kurile-Kamchatka-Eastern Hokkaido	7	5	4	3
9	North Honshu-Sea of Japan-Manchuria	0	3	0	3
10	Central Honshu-Izu-Bonin	1	3	1	2
11	Ryukyu-Taiwan	1	0	0	0
12	Philippines-Celebes	0	1	0	1
13	Sunda	1	4	0	3
14	Burma	1	0	0	0
15	Hindu-Kush	2	0	2	0
16	Spain	0	1	0	1
Total		35	29	19 54%	22 76%
		64		41 (64%)	
<i>I</i> , $100 \leq h < 300$ km		<i>D</i> , $h \geq 300$ km			

sequently, about sixty-four percent of deep-focus earthquakes ($h \geq 100$ km) were identified with the multiple shock. This evidence shows that for deep-focus earthquakes and intermediate-depth earthquakes the occurrence of the multiple shock is not accidental but essential in the rupture process in the focal region.

Oike⁹⁶⁾ showed that multiplets with a origin time difference less than 10 days and with spatial separation of about 30 km, most of which are after-shocks, have the following regional characteristics: the multiplets are frequently observed in the intermediate zones of the South Sandwich Islands, Colombia, Celebes Island, the Banda Sea, New Guinea, the New Hebrides Islands and the Hindu Kush, and in the deep zones of South America, the Java-Banda Sea, the Santa Cruz Islands and the Fiji Islands; on the contrary these are hardly observed in Central America, Kurile-Japan, the Izu-Marianas and the Ryukyu regions. However, the occurrence of the multiple shocks with a remarkably short time interval shows no regional characteristics.

3.2 Multiple shock analysis

Method of analysis

Differences in the origin times and hypocenter locations of earthquakes are determined by the usual method (Method I; Isacks et al.⁴⁰); Oike⁴¹); Fukao³⁰). Consider the i -th and j -th earthquakes separated by l km in distance and occurring with the difference of τ_0 in origin time (Fig. 36). Here we assume that the i -th earthquake is the first shock. Arrival time difference of phases for the i -th and j -th earthquakes, τ_{ij} , is approximately given by:

$$\tau_{ij} = \tau_0 - \frac{l}{V_{p,s}} \cos \theta \tag{17}$$

where θ is the angle between the line joining hypocenters E_i and E_j and the direction of seismic ray to the observation point, and $V_{p,s}$ the P and S wave velocities at the source. If the orientation (ϕ^* , δ^*) of l is chosen correctly and there is no contamination of waves due to noise or error in the seismograms, the observed values τ_{ij} should be given on a straight line on a τ_{ij} vs. $\cos \theta$

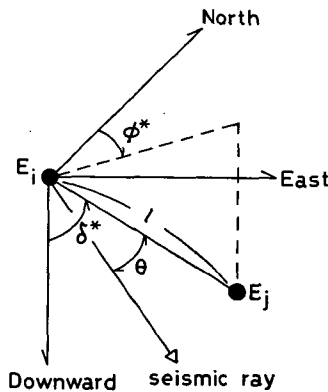


Fig. 36 Coordinate system and notations used in the calculation. E_i and E_j are hypocenters of the i -th and j -th shocks. ϕ^* and δ^* are strike and plunge of the line joining two hypocenters E_i and E_j . θ is the angle between the line $E_i E_j$ and the direction of seismic ray for the observation point.

plot. The standard deviation σ of the difference between the observed and calculated values of τ_{ij} is computed for different orientations of l , and the orientation that gives the best fit or the smallest standard deviation is taken as a solution. The intercept of the straight line gives the value of τ_0 and the

gradient of that line gives the value of l . The orientation of the line l is varied by 2° -dip intervals and 2° -azimuth intervals in obtaining the best fit. To obtain the solution being highly accurate and of high resolution power, the wide range in the value of $\cos \theta$ will be required. For the requirement not only P waves but also pP waves are used in the analysis. The solution obtained from the P waves is examined whether it explains the observed arrival time differences of S waves or not, if possible.

When the j -th earthquake occurs at a point just under (or up) the i -th earthquake, θ corresponds to the incident angle (or its supplement angle) of a seismic ray at the focus. For such earthquake, τ_{ij} shows no appreciable azimuthal variation because the term $\cos \theta$ hardly changes at different epicentral distances in the far-field; for example, $\cos \theta = 0.766$ at $\Delta = 40^\circ$ and $\cos \theta = 0.906$ at $\Delta = 80^\circ$ for the earthquake with $h = 200$ km. Solutions obtained from τ_{ij} in the narrow range of the values of $\cos \theta$ are less reliable. To such τ_{ij} another method for the analysis must be applied. When we recognize that the observed values of τ_{ij} show no appreciable azimuthal variation, we obtain two equations of (17) corresponding to two different waves such as P and pP waves or P and S waves. For the waves the average values of τ_{ij} and θ are used. Then we solve the simultaneous equations to determine the difference in origin times and relative hypocenter location. This is the second method (Method II).

We define the apparent rupture velocity V_a (Fukao³⁰) as

$$V_a = l/\tau_0. \quad (18)$$

On discussion about the rupture mechanism of the multiple shock the seismic moment of the first shock will be used. The seismic moment can be obtained from the P wave source time function using equation (13). However, for determining the seismic moment in the later analysis we use a simple method as follows. A double-couple point source with a moment rate function $M(t)$ is assumed as a source model. The moment rate function $M(t)$ is given by a step function which corresponds to that $s(t) = 1.0$ at $t = 0$ and $s(t) = 0$ at $t \neq 0$ in equation (8). Figure 37 shows the seismic moment M_0^* with which the double-couple point source is assumed to radiate P waves with the peak amplitude of 1 cm in the vertical component of the WWSSN long-period seismogram ($T_p = 15$ sec, $T_g = 100$ sec and $Mag = 1500$). These seismic moments were computed using equations (1) and (8). In the computation the radiation pattern coefficient R_p was taken as 1.0. Using M_0^* in this figure we

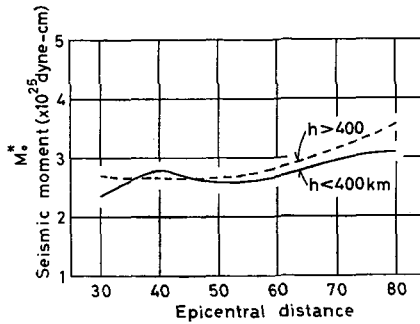


Fig. 37 Seismic moments of the double-couple point source which radiates the P waves with the peak amplitude of 1 cm in the vertical component of the WWSSN long-period seismogram ($T_p=15$ sec, $T_g=100$ sec and $Mag=1500$).

can obtain the seismic moment M_0 from the observed peak amplitude of P wave in the vertical component, A_p (in cm), by correcting for the effect of the radiation pattern as

$$M_0 = M_0^* \frac{A_p}{R_p} \tag{19}$$

Multiple shock analyses were made for nine deep-focus earthquakes which are listed in Table 13. In the present paper, the multiple shock analysis is presented in detail for two earthquakes, that is, the Hindu-Kush earthquake of July 30, 1974, and the Sea of Okhotsk earthquake of September 5, 1970. For the multiple shock analyses of the other earthquakes, the reader refer to Sasatani⁶⁶).

Hindu-Kush earthquake of July 30, 1974 (h=210 km)

Figure 38(a) shows examples of seismograms in which P and pP waves of this earthquake are recorded. As can be seen in the figure, a remarkable phase (referred to as P_2 in the figure) follows the first P wave about 6 sec later and another remarkable phase (referred to as pP_2 in the figure) follows the first pP wave about 8.5 sec later. Figure 38(b) shows examples of seismograms in which S wave of this earthquake is recorded. In the seismograms, a remarkable phase which is marked with S_2 in the figure is discernible 4–8 sec after the first S arrival. The travel-time differences shown in Fig. 35 show that these remarkable phases following the main phases cannot be identified with any expected phases except PcP wave at distances of about 80° . This suggests that the remarkable phases are not generated by the

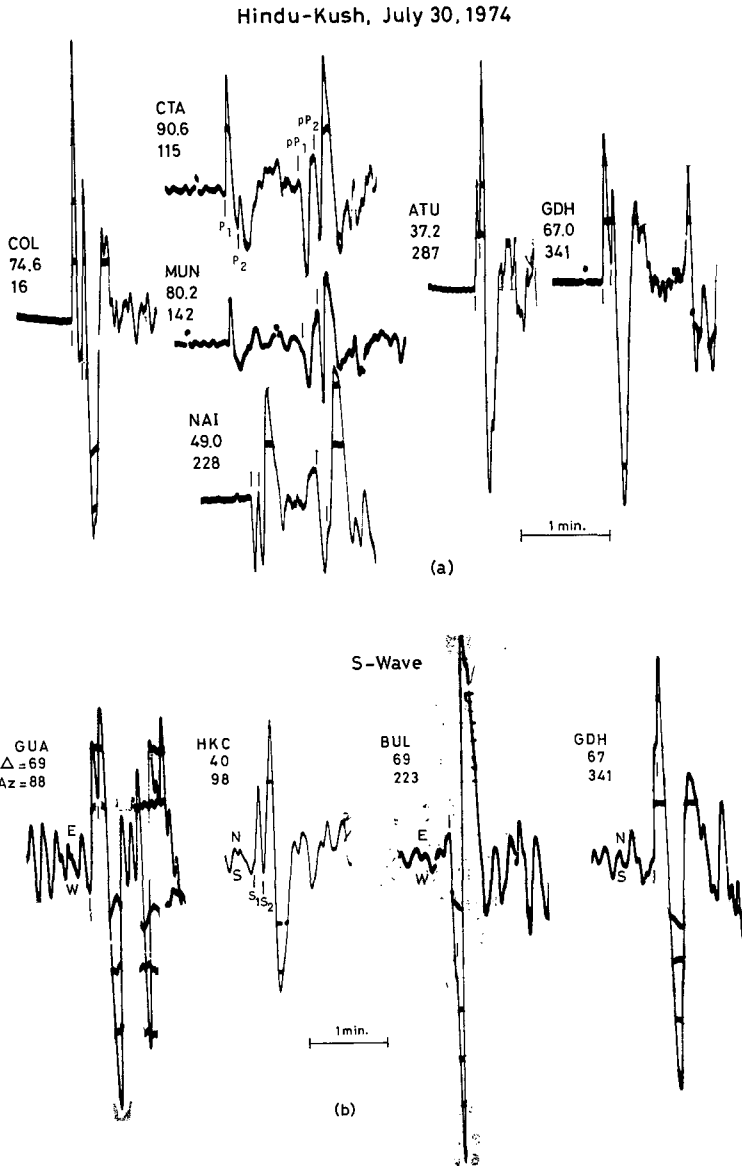


Fig. 38 WWSSN long-period seismograms of P and pP waves (a) and S waves (b). The numbers attached to each station code indicate the epicentral distance (upper) and the epicenter-to-station azimuth (lower) in degrees. Note the multiple arrivals; tick marks indicate the first and second arrivals for each wave.

Table 11 Difference of arrival times between P_2 and P_1 phases and between pP_2 and pP_1 phases, and seismic moment for the Hindu-Kush earthquake.

Station	Δ deg.	Az deg.	i_p deg.	P_2-P_1 sec	pP_2-pP_1 sec	$M_0, 10^{26}$ dyne-cm
AAE	40	235	39	5.6	6.8	—
AKU	57	330	33	5.7	—	0.87
ALQ	109	358	20	6.4	—	—
ATU	37	287	40	3.6	—	1.42
BKS	105	11	20	6.5	—	—
BLA	102	337	20	6.2	—	—
BUL	69	223	28	—	8.1	—
COL	75	16	26	6.8	—	—
COP	43	315	38	5.9	—	—
COR	98	10	21	6.6	—	—
CTA	91	115	21	8.4	9.4	—
ESK	52	316	35	5.2	—	1.00
GDH	67	341	29	5.8	—	1.23
GUA	69	88	28	8.0	—	1.38
HNR	95	98	21	8.2	—	—
KEV	41	338	39	6.0	—	1.36
KON	45	321	38	5.2	—	1.29
LON	96	9	21	6.1	—	—
SDB	74	238	26	4.7	8.8	—
MAT	53	68	35	7.8	—	—
SNG	40	130	39	7.8	—	1.67
MUN	80	142	24	—	10.0	—
NAI	49	228	36	5.4	7.6	1.17
OXF	107	343	19	5.8	—	—
PDA	73	305	27	5.4	—	—
PTO	60	301	32	5.0	—	1.10
RAB	86	98	22	7.4	8.7	—
STU	46	306	37	4.6	7.6	1.22
VAL	57	313	33	5.4	—	1.10
WES	94	333	21	5.6	—	—

i_p =take-off angle measured from downward vertical.

Av. 1.23

reflected waves but generated by the second shock.

Arrival time differences τ_{ij} between the first and the second P phase or those between the first and the second pP phase or both were measured at thirty stations. These are presented in Table 11. Figure 39 shows plots of τ_{ij} for both P and pP waves versus epicenter-to-station azimuth. In the figure azimuthal variation of τ_{ij} is observed.

According to Method I, least-squares fit was applied to these time differences of the first and second arrivals. Figure 40 shows distribution of the standard deviation of τ_{ij} for different orientations of l on the equal-area projection. The least squares solution obtained is shown in Fig. 41. The solution is that $\phi^*=278^\circ$, $\delta^*=66^\circ$, $\tau_0=7.61$ sec, $l/V_p=3.21$ sec, and $\sigma=0.482$

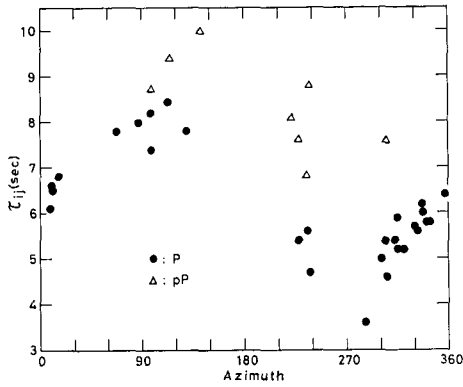


Fig. 39 Plot of τ_{ij} for P and pP waves versus epicenter-to-station azimuth.

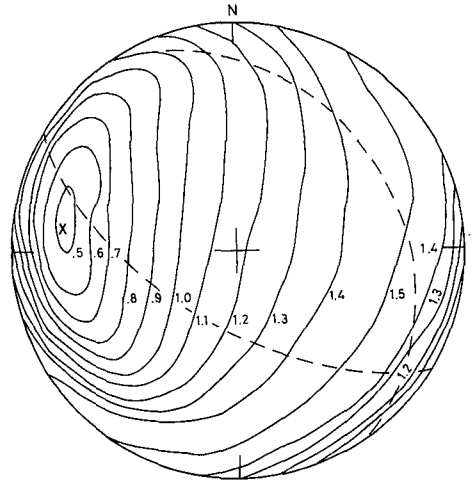


Fig. 40 Distribution of the standard deviation of τ_{ij} on the equal-area projection (lower hemisphere). The value associated with each contour is in seconds. The cross represents the location of the second shock while the location of the first shock is at the center of the plot. The dashed curves are nodal planes of the first shock.

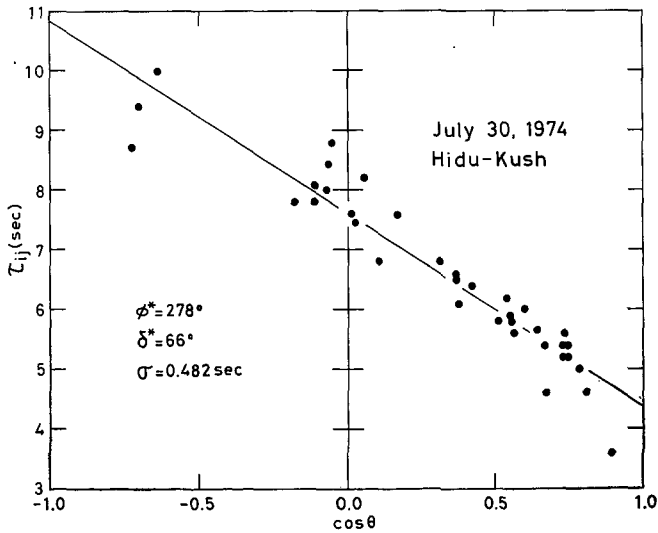


Fig. 41 Least-squares fit of the arrival time differences between the first and second phases of P and pP waves.

sec. If a P wave velocity of 8.3 km/sec is assumed in a region around the source, the distance between the two foci is obtained to be 26.6 km. The apparent rupture velocity was determined to be 3.50 km/sec. Since a velocity of S wave in a region around the source may be assumed to be 4.6 km/sec, the apparent rupture velocity amounts to about 76% of the S wave velocity.

The solution obtained from the P waves was confirmed by arrival time differences of S waves. For example, at stations GUA, HKC, BUL and GDH the arrival time differences expected from the solution of P waves are 8.0, 9.1, 4.1 and 4.4 sec, respectively, which closely agree with the observed arrival time differences at these stations: 7 sec (GUA), 8 sec (HKC), 4 sec (BUL) and 4 sec (GDH). This agreement implies the solution obtained from P waves being reliable.

Figure 42 shows the focal mechanism solution for the first shock. The initial motions of the second P phase at most stations were obtained to be much the same as those of the first P phase. This implies that the mechanism solution for the second shock is similar to that for the first shock. The location of the second shock is plotted in the focal mechanism solution of Fig. 42, in which the location of the first shock is placed on the center of the solution. This hypocenter location is very close to or just on a nodal plane with a dip direction of 212° and a dip angle of 63° .

The seismic moment of the first shock was determined as $M_0 = 1.2 \times 10^{26}$ dyne-cm (Table 11).

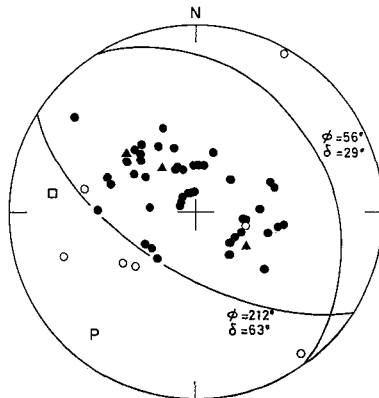


Fig. 42 Focal mechanism solution for the first shock. Symbols are the same as in Fig. 10. The square represents the location of the second shock while the location of the first shock is at the center of the plot.

Sea of Okhotsk earthquake of September 5, 1970 ($h=560$ km)

Examples of seismograms of P and pP waves of this earthquake are shown in Fig. 43. Two remarkable phases are observed; the first remarkable phase arrives about 3.5 sec later of the first P arrival and the second one, about 7.5 sec later of the first pP arrival. Arrival time differences between the first P or pP wave and each of the remarkable phases, τ_{ij} , are shown in Fig. 44 as a function of epicenter-to-station azimuth (also see Table 12).

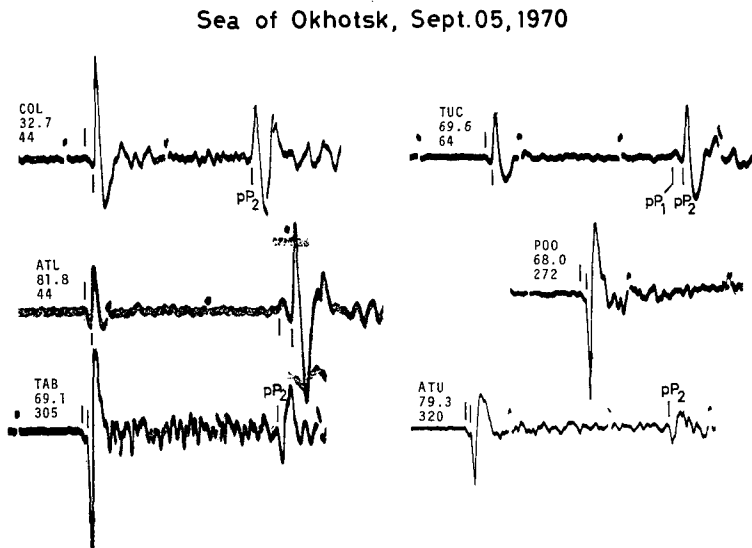


Fig. 43 WWSSN long-period seismograms of P and pP waves. Notations are the same as in Fig. 38.

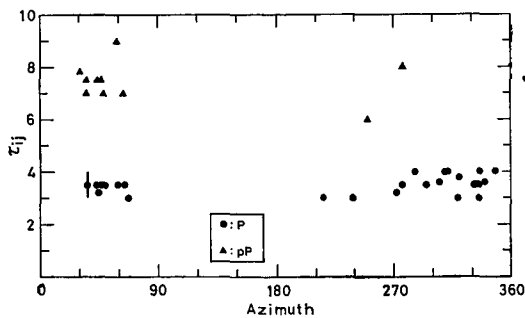


Fig. 44 Plot of τ_{ij} for P and pP waves versus epicenter-to-station azimuth.

Table 12 Difference of arrival times between P_2 and P_1 phases and between pP_2 and pP_1 phases, and seismic moment for the Sea of Okhotsk earthquake.

Station	Δ deg.	Az deg.	i_p deg.	P_2-P_1 sec	pP_2-pP_1 sec	$M_0, 10^{25}$ dyne-cm
ALQ	70	59	35	3.5	9.0	0.43
ATL	82	44	30	3.2	7.5	0.57
ATU	79	320	31	3.8	—	0.51
BKS	59	67	40	3.0	—	—
CHG	53	251	44	—	6.0	—
COL	33	44	55	3.5	—	0.57
COP	67	336	36	4.0	—	—
FLO	75	46	33	3.5	—	0.72
GEO	80	36	30	3.5	—	—
HLW	83	311	29	4.0	—	0.52
IST	75	319	33	3.0	—	0.55
JER	80	309	30	4.0	—	—
KON	64	340	38	3.6	—	—
MAT	18	216	68	3.0	—	—
NDI	59	277	41	3.5	8.0	—
NUR	60	333	40	3.5	—	0.68
OXF	79	47	31	3.5	7.5	—
POO	68	272	36	3.2	—	—
QUE	64	286	38	4.0	—	—
SCP	78	36	31	3.5	7.0	—
SEO	23	239	62	3.0	—	—
SHA	82	49	29	3.5	7.0	—
SHI	72	295	34	3.5	—	0.88
STU	74	335	33	3.0	—	—
TAB	69	305	36	3.6	—	1.10
TRI	76	331	32	3.5	—	0.85
TUC	69	64	35	3.5	7.0	—
UME	58	337	41	3.5	—	—
VAL	75	348	33	4.0	—	—
WES	79	31	31	—	7.8	—

Av. 0.67

They show no appreciable azimuthal variation. Since $\tau_{ij}(P) < \tau_{ij}(pP)$, it is inferred that the second shock occurred just beneath the first shock.

We applied the second methods (Method II) to obtain the difference in origin times and the relative hypocenter location. Using average values of τ_{ij} for P and pP waves, $V_p=10$ km/sec and the average value of incident angles ($i_p=37^\circ$ and $i_{pP}=143^\circ$), we have simultaneous equations in τ_0 and l as:

$$3.5 = \tau_0 - \frac{l}{10} \cos 37^\circ \quad \text{for P waves,}$$

$$7.4 = \tau_0 - \frac{l}{10} \cos 143^\circ \quad \text{for pP waves.}$$

Solving the equations, we obtained $l=24.4$ km and $\tau_0=5.5$ sec. The apparent rupture velocity was determined to be 4.4 km/sec, which is about 80% of V_s (5.5 km/sec).

This result was confirmed by the arrival time differences between P and pP waves for each shock as shown in Fig. 45. This figure clearly shows that the second shock occurred deeper than the first shock. Moreover, the travel time differences between P and pP waves and its gradient to focal depth allow us to estimate the approximate location of the second shock. As $d(pP-P)/dh \approx 0.175$ sec/km and $(pP_2-P_2)-(pP_1-P_1) \approx 4$ sec at $\Delta=80^\circ$, we obtained $l=23.3$ km. This value is almost consistent with the result obtained above.

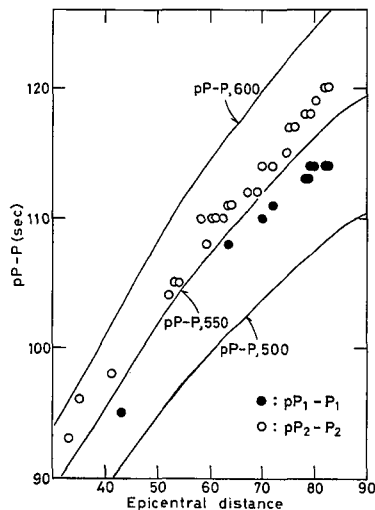


Fig. 45 Travel time differences between P and pP waves for the first and second shocks. Theoretical curves are taken from Herrin⁹⁴).

The multiple-shock analysis was also applied to this earthquake by Strelitz⁹⁷). He obtained that $l=23.0$ km and $\tau_0=5.16$ sec. Our result is approximately consistent with his result.

Figure 46 shows the focal mechanism solutions for the first and second shocks. The two solutions are quite different from each other. The location of the second shock is evidently separated from both of the nodal planes of the first shock; the second shock is located to be very close to the P axis.

The seismic moment of the first shock was determined to be 6.7×10^{24} dyne-cm (Table 12).

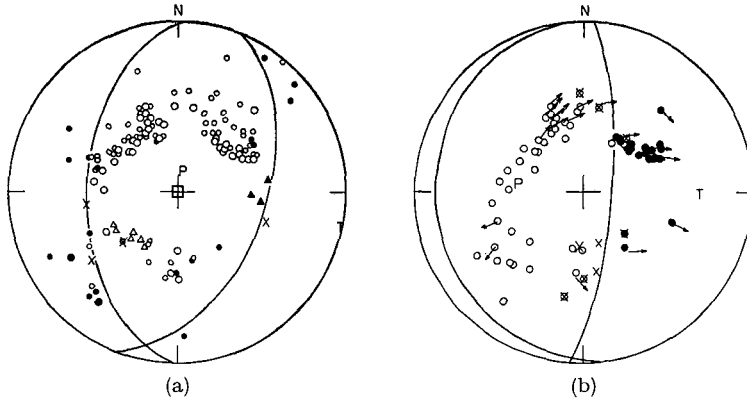


Fig. 46 Focal mechanism solutions for the first shock (a) and the second shock (b). Symbols are the same as in Fig. 10. In (a), small symbols are the data from ISC.

Summary of the results

In Table 13 the results of the multiple-shock analyses are summarized for eighteen earthquakes; the results for 9 earthquakes are obtained by the present author and those for 9 earthquakes are quoted from other published papers. For the multiple shocks being composed of several shocks, the result for shocks in the early stage (the second shock, at most the third shock) is given because of the high accuracy of the analysis for these shocks. For some multiple shocks, the analysis was made on an ambiguous phase in later arrivals or on the waves recorded at stations which are located in a narrow range of values of $\cos \theta$. These multiple shocks are labelled as a quality B in the Table.

Figure 47 shows the focal mechanism solutions for the first and second shocks, in which the location of the second shock is also plotted. The focal mechanism solution for the second shock is nearly the same as that for the first shock for most cases, while the mechanism solution for the second shock of multiple shocks 2 and 10 is extremely different from that for the first shock. As shown in the figure the location of the second shock is obtained to be very close to one of the two nodal planes of the first shock for earthquakes 1, 3, 4, 5, 7, 8, 15, 16, 17 and 18. However, this is not the case for the other earthquakes. Especially for earthquakes 2, 9, and 10, the location of the

Table 13 Results of

No.	Date	Epicenter		Depth km	m_b	l km
		Lat.	Long.			
1	Mar. 29, 1954	36.98°N	3.54°W	630	7.1	19.0
2	Aug. 15, 1963	13.80°S	69.33°W	546	7.5	46.9
3	Nov. 09, 1963	8.93°S	71.56°W	577	7.0	26.7
3*	"	"	"	"	"	31.0
4	Jun. 22, 1966	7.21°S	124.69°E	523	6.1	17.9
5	Jan. 19, 1969**	14.89°S	167.22°E	114	6.2	23.8
6	Feb. 10, 1969	22.57°S	178.76°E	635	6.0	24.8
7	Mar. 31, 1969	38.49°N	134.52°E	397	5.7	12.3
8	July 31, 1970	1.46°S	72.56°W	653	6.5	17.4
9	Aug. 30, 1970	52.36°N	151.63°E	643	6.5	0.0
9*	"	"	"	"	"	0.0
10	Sept. 05, 1970**	52.28°N	151.49°E	560	5.7	24.4
11	Dec. 07, 1970	29.70°N	140.11°E	183	6.0	8.2
12	Nov. 21, 1971	11.87°S	166.55°E	119	6.5	14.2
13	Mar. 30, 1972	25.69°S	179.58°E	479	6.1	10.4
14	Apr. 04, 1972	7.47°S	125.56°E	375	6.1	12.8
15	Sept. 10, 1973	42.45°N	130.91°E	565	6.0	12.3
16	Sept. 29, 1973	41.89°N	130.87°E	575	6.5	47.3
17	July 30, 1974	36.42°N	70.76°E	209	6.3	26.6
18	Mar. 07, 1978	31.91°N	137.55°E	432	6.5	23.7

l =space interval; τ_0 =difference in origin times; V_a =apparent rupture velocity; SD=
 **=earthquake analyzed by using Method II (the other earthquakes are analyzed by
 (5)=Sasatani⁶⁸); (6)=Furumoto⁸⁰); (7)=Strelitz⁹⁷); (8)=Koyama³⁴); (9)=Koyama³⁵);

second shock is obtained to be rather close to the P axis. As the dislocation theory demonstrates that the stress concentration occurs at and near the edge of the fault plane (e.g., Rybicki⁶⁸), the second shock for the former multiple shocks may be interpreted as being caused by the stress concentration due to the rupture propagation of the first shock. For the latter multiple shocks, however, the second shock does not seem to be caused by the stress concentration due to the rupture propagation of the first shock, because the location of the second shock deviates from one of the two nodal planes of the first shock.

Figure 48 shows the distance between two hypocenters, l , plotted against the difference in origin times, τ_0 . The ratio of l to τ_0 gives the apparent rupture velocity. From the figure the range in which the apparent rupture velocities change is roughly estimated to be from 2.0 km/sec to 4.5 km/sec. Figure 49 shows the apparent rupture velocity V_a plotted against the S wave velocity V_s at the focus. The ratio of V_a to V_s ranges from 25% to 80%. The upper limit of the ratio roughly agrees with the ratio of the actual rupture velocity to the S wave velocity at the focus as is found in section

multiple-shock analysis.

τ_0 sec	V_a km/s	SD sec	TYPE	M_0 10^{25} dyne-cm	Q	Ref.
4.3	4.3	0.36	2A	21.0	A	(1)
15.8	3.0	—	2B	25.4	A	(2)
12.9	2.1	0.22	2A	164	A	(3)
13.9	2.2	0.42	2A	164	A	(3)
5.6	3.2	0.90	2B	1.4	B	(4)
12.6	1.9	—	2B	7.2	A	(5)
6.0	4.1	0.48	2B	10.5	B	(5)
3.9	3.2	0.60	2B	0.5	A	(4)
5.4	3.2	—	2A	160	B	(6)
4.0	—	—	1A	36.7	B	(5)
5.0	—	—	1A	36.7	B	(5)
5.5	4.4	—	2B	0.7	A	(5), (7)
4.5	1.8	0.49	2B	3.5	A	(5)
7.2	2.0	0.57	2B	17.4	A	(5)
5.7	1.8	0.57	2B	4.3	A	(5)
9.5	1.4	0.70	2B	6.4	B	(5)
3.8	3.3	0.39	2A	8.6	A	(8)
12.9	3.7	0.45	2B	139	A	(9)
7.6	3.5	0.48	2B	13.7	A	(5)
6.9	3.4	—	2B	1.0	A	(10)

standard deviation; M_0 =seismic moment for the first shock; Q=Quality; *=3-rd shock; using Method I); (1)=Chung and Kanamori⁴⁴); (2) Sudo⁸⁸); (3)=Fukao³⁰); (4) Oike⁷⁶); (10)=Sudo⁸⁹).

2.4. This agreement supports the mechanism of the multiple shock in which the second shock is caused by the stress concentration due to the rupture propagation of the first shock. For the multiple shocks in which the second shock is located on neither of the nodal planes of the first shock, the second shock may be triggered by the stress disturbance due to S wave propagated from the source area of the first shock.

3.3 Mechanism of deep multiple shocks

In this section we shall discuss the rupture mechanism not only for multiple shocks with a remarkably short time interval but also for deep after-shocks.

Classification of deep multiple shocks

It is reasonable to consider that the stress disturbance is necessary to trigger the earthquakes. There are many evidences of triggering of earthquakes; for example, earthquakes are known to be triggered by some artificial

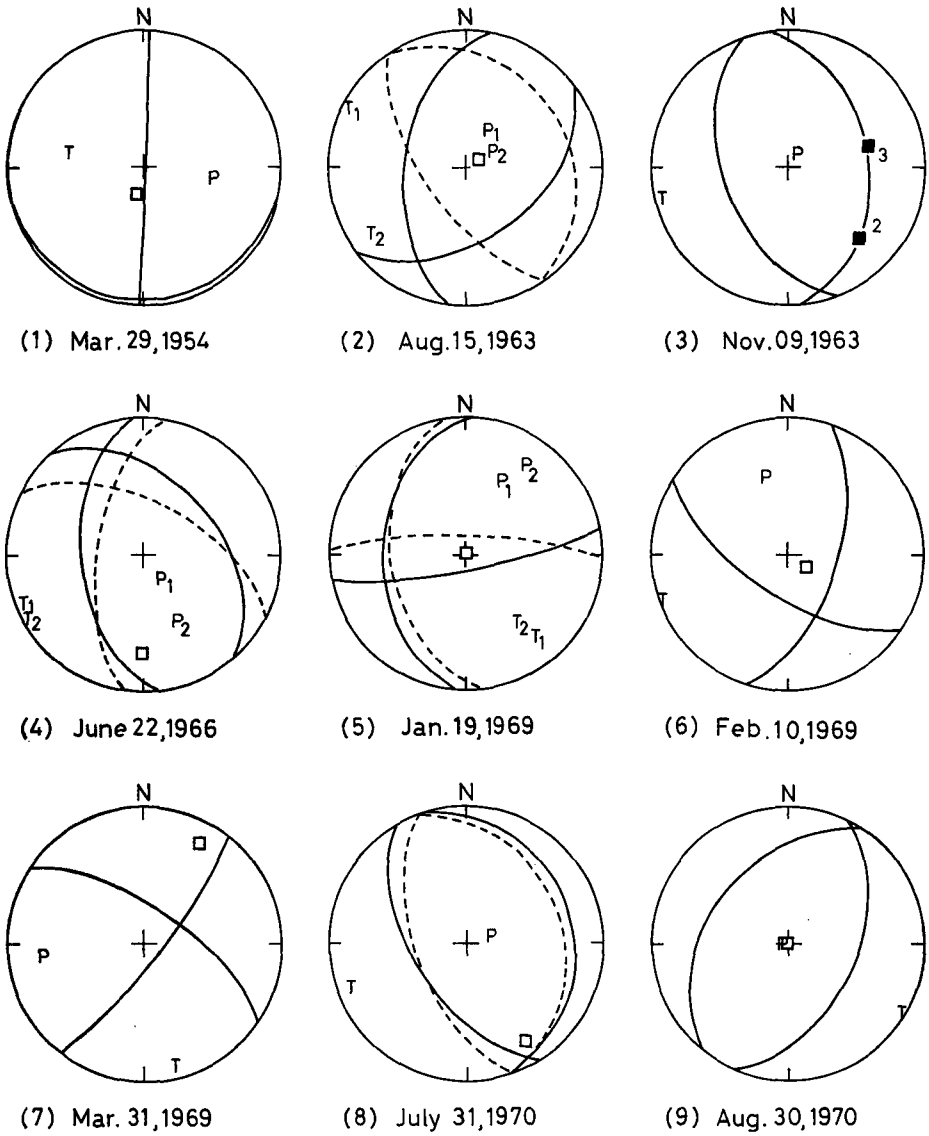
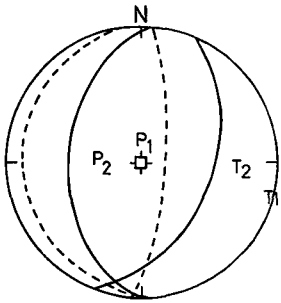
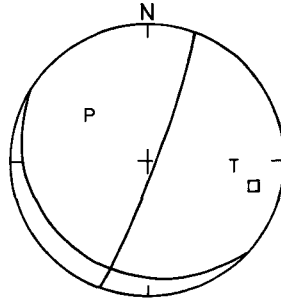


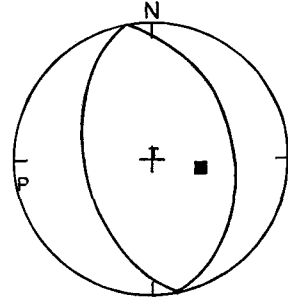
Fig. 47 Focal mechanism solutions and locations of the second shock and the third shock (only for earthquakes (3) and (9)). Equal-area projection of the lower hemisphere of the focal sphere is used. The solid curves are nodal planes of the first shock and the dashed curves are nodal planes of the second shock. When the mechanism solution for the second shock is similar to that for the first shock, only nodal planes of the first shock are drawn. The open square represents the



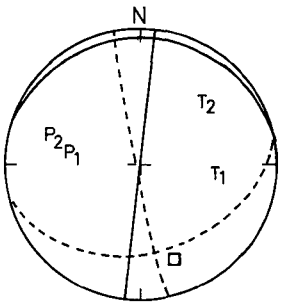
(10) Sep. 5, 1970



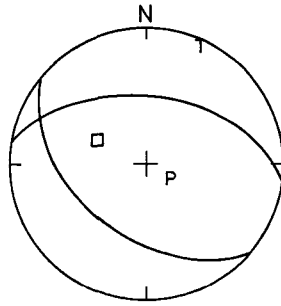
(11) Dec. 7, 1970



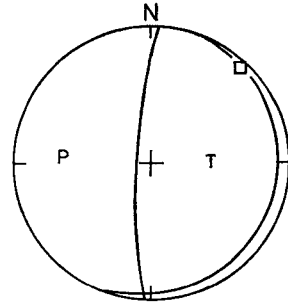
(12) Nov. 21, 1971



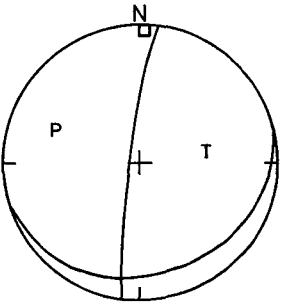
(13) Mar. 30, 1972



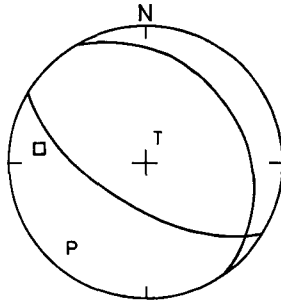
(14) Apr. 4, 1972



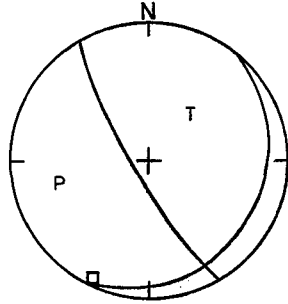
(15) Sep. 10, 1973



(16) Sep. 29, 1973



(17) July 30, 1974



(18) Mar. 7, 1978

location of the second shock on the lower hemisphere; and the filled square represents the location of the second shock on the upper hemisphere (the location is projected onto the lower hemisphere through the center of the focal sphere). P and T represent the axis of compression and the axis of tension, respectively.

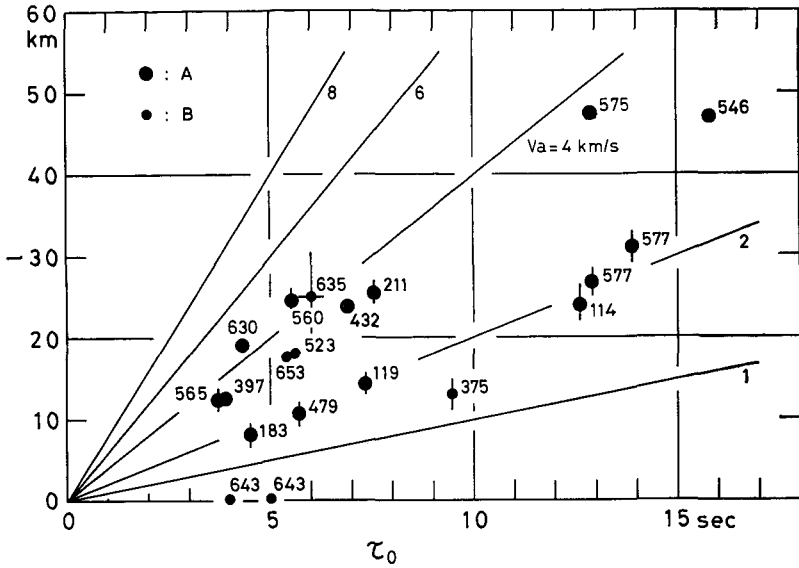


Fig. 48 Relation between l (distance between two hypocenters) and τ_0 (difference in origin times). The numbers attached to each shock indicate the focal depth in km. The straight lines give the apparent rupture velocities. Large symbols indicate reliable solutions (quality A), and small symbols, less reliable solutions (quality B).

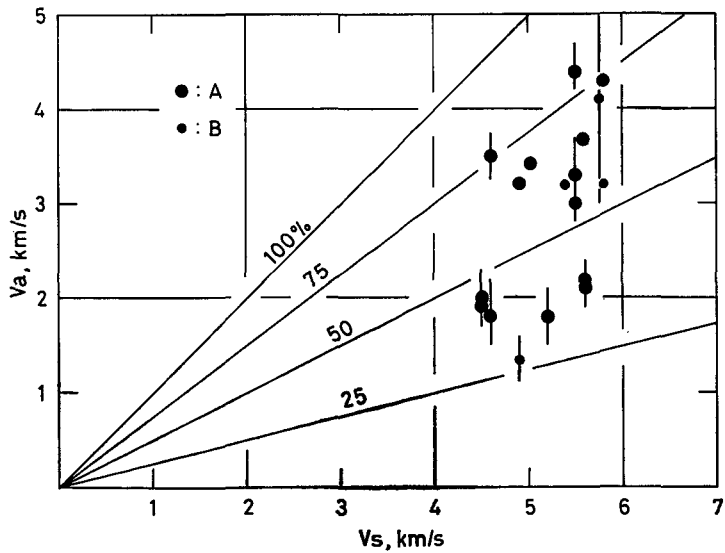


Fig. 49 Relation between V_a (apparent rupture velocity) and V_s (S wave velocity at the focus). The straight lines give the percent of V_a to V_s .

operations such as underground nuclear explosions (Ryall and Savage¹⁰⁰), the filling of large reservoirs (Gough and Gough¹⁰¹), fluid injection in deep wells (Raleigh et al.¹⁰²; Ohtake¹⁰³; Fletcher and Sykes¹⁰⁴), and crustal off-loading (Pomeroy et al.¹⁰⁵). Triggering of earthquakes has also been found in the laboratory experiments. Auer and Berckhemer⁶² carried out fracture experiments with two-dimensional plates of plastics. Their experiments were to study a triggered fracture process using a high energy rubidium pulse laser as a source for the trigger energy. A result they obtained is that it is possible to initiate fracture even in the stress range 0.2–0.8 of the strength of the material. Brune¹⁰⁶ reported in his stick-slip experiments with foam rubber that the fault is triggered by decreasing the normal stress.

The stress field around the focus after the occurrence of one earthquake is disturbed by the dynamic stress due to transient seismic body waves and by the static stress. It is widely accepted that aftershocks are caused more or less by the static stress concentration due to the main shock. For deep-focus earthquakes there are two types in occurrence of aftershocks as shown in section 2.4, that is, TYPE 1A and TYPE 1B: TYPE 1A is that aftershocks occur near the fault plane of the main shock and TYPE 1B is that aftershocks occur considerably apart from the fault plane of the main shock.

For multiple shocks with a remarkably short time interval, two types of the dynamic stress disturbance to trigger earthquakes, which are referred to as TYPE 2A and TYPE 2B, are suggested in the last section. TYPE 2A is that the second shock of the multiple shock is an immediate result of the rupture propagation of the first shock. In this case, the location of the second shock is most likely to be on one of the nodal planes of the first shock, and the apparent rupture velocity is nearly the same as the true rupture velocity, for example, $0.8 V_s$. TYPE 2B is that the second shock is caused by the stress disturbance due to S wave generated from the first shock. In this case, the location of the second shock may or may not be on one of the nodal planes of the first shock, and the apparent rupture velocity is nearly the same as or slightly less than the S wave velocity in a region around the focus. Schematic illustration of four types of the multiple shocks is shown in Fig. 50.

When the second shock is located on one of the nodal planes of the first shock and the apparent rupture velocity is 70–80% of the S wave velocity in a region around the focus, the second shock is usually considered to be the result of the rupture propagation of the first shock; the apparent rupture velocity corresponds to the true rupture velocity, and the nodal plane of the

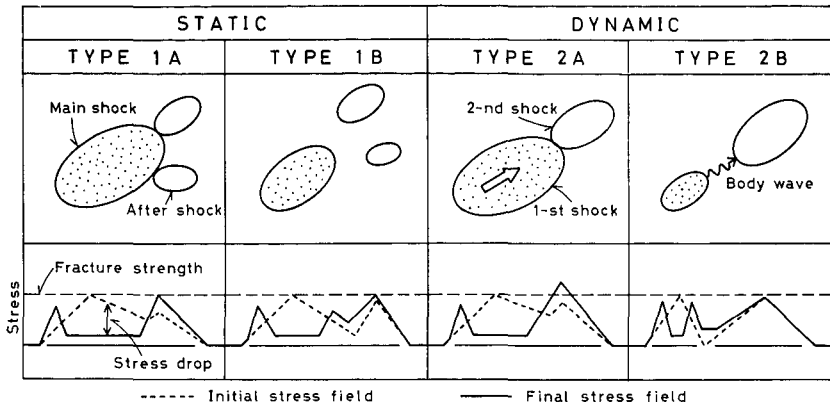


Fig. 50 Schematic illustration of four types of multiple shocks (upper) and the spatial distribution of stresses before and after the first shock for each type of the multiple shocks (lower).

first shock, on which the second shock is located, is selected as the actual fault plane (Oike⁴¹); Fukao³⁰); Chandra²⁸); Chung and Kanamori⁴⁴). However, if the fault dimension of the first shock is much less than the distance between two hypocenters, the second shock is not the immediate result of the rupture propagation of the first shock, but the result of the stress disturbance due to S wave propagated from the source area of the first shock. Then the fault dimension of the first shock provides the key to the classification of the multiple shocks.

The multiple shock can be classified into one of the four types depending on the characteristics described in Table 14. In the Table, l is the distance between two hypocenters and L^* the fault dimension of the first shock.

For small earthquakes ($m_b < 6.0$), it is a little difficult to estimate the fault dimension using the WWSSN long-period seismograms. However, if the seismic moment is given, we can roughly estimate the fault dimension of the first shock. Here we assume the following similarity conditions: (1) W^*/L^* is constant, where W^* is the fault width and L^* the fault length, and (2) the stress drop is constant at a given depth. The first assumption seems reasonable for most earthquakes and W^*/L^* is taken as 1/2 (Kanamori and Anderson,⁶⁹); Abe⁷⁰); Geller⁷¹). The second assumption is approximately valid for large deep-focus earthquakes as shown in Fig. 31 as well as for most shallow earthquakes (Aki¹⁰⁷); Kanamori and Anderson⁶⁹); Abe⁷⁰). From these assumptions, equation (16) provides that

Table 14 Classification of the multiple shocks.

TYPE	Location of the second shock	Relation between l and L^*	Relation between V_a and V_r
TYPE 1A	be on one of nodal planes of the first shock	$l \lesssim L^*$	$V_a \ll V_r$
TYPE 1B	may or may not be on one of nodal planes of the first shock	$l > L^*$	$V_a \ll V_r$
TYPE 2A	be on one of nodal planes of the first shock	$l \lesssim L^*$	$V_a \approx V_r$
TYPE 2B	may or may not be on one of nodal planes of the first shock	$l > L^*$	$V_a \approx V_r$

l =space interval; L^* =fault dimension of the first shock; V_a =apparent rupture velocity; V_r =rupture velocity.

$$L^* = \sqrt{2\pi} \left(\frac{7}{16} \frac{M_0}{\Delta\sigma} \right)^{1/3} \tag{20}$$

The relation between the fault dimension L^* and the seismic moment M_0 is shown in Fig. 51. In the figure the constant stress drop at a given depth range is taken as about 160 bars for $100 < h < 200$ km and 500 (± 300) bars for $300 < h < 650$ km based on the results in section 2.4. The fault dimension of the first shock can be estimated from this relation if the seismic moment is given.

For many intermediate and deep earthquakes occurring in the years from 1964 to 1969, Oike⁷⁶⁾ determined the space intervals between the main

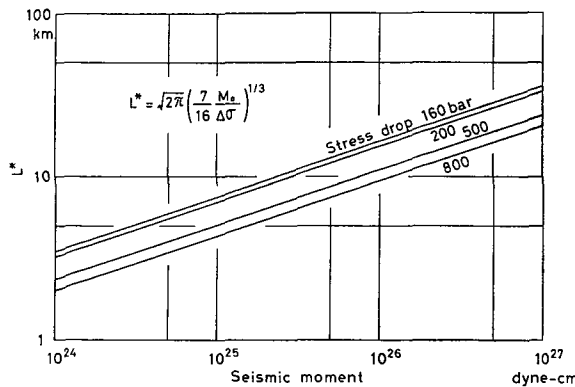


Fig. 51 Relation between L^* (fault dimension) and M_0 (seismic moment).

shock and the aftershocks. In the present study these aftershocks were classified into TYPE 1A or TYPE 1B depending on the characteristics described in Table 14. Although the seismic moments of these main shocks were not determined from amplitudes of the WWSSN long-period seismograms, the seismic moments were roughly estimated from the magnitude (m_b) using the empirical relation between the seismic moment and the earthquake magnitude as shown in Fig. 52. The results of the classification for twenty-two earthquakes are listed in Table 15, in which the results for the earthquakes studied in chapter 2 are also listed. Among these earthquakes, eight earthquakes were classified into TYPE 1A and fourteen earthquakes, into TYPE 1B. Table 15 shows that the deep aftershocks of TYPE 1B occur frequently.

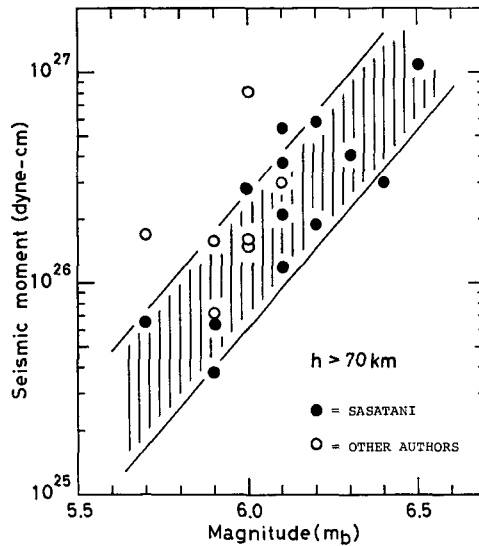


Fig. 52 Relation between seismic moment and body wave magnitude for deep-focus earthquakes.

Each multiple shock with a remarkably short time interval was classified into one of the four types. The results for eighteen multiple shocks are listed in Table 13. Thirteen multiple shocks were classified into TYPE 2B and five multiple shocks, into TYPE 2A. Table 13 clearly shows that TYPE 2B is most frequent for the occurrence of the multiple shocks.

In the classification of multiple shocks into TYPE 2B, we have paid no

Table 15 Classification of deep aftershocks.

No.	Date	Lat.	Long.	h , km	m_b	TYPE	Ref.
1	Nov. 28, 1964	7.90°S	71.29°W	650	5.3	1A	(1)
2	Dec. 09, 1964	27.40°S	63.23°W	578	5.8	1B	(1)
3	Dec. 28, 1964	22.13°S	179.62°W	577	5.7	1B	(1)
4	Jan. 02, 1965	19.11°N	145.61°E	141	5.7	1A	(1)
5	Mar. 14, 1965	36.42°N	70.73°E	205	6.4	1A	(1)
6	Apr. 10, 1965	17.84°S	178.70°W	535	5.7	1B	(1)
7	Feb. 03, 1966	0.11°N	123.52°E	180	5.7	1B	(1)
8	Mar. 17, 1966	21.08°S	179.15°W	627	5.9	1A	(1)
9	May 01, 1966	8.32°S	74.24°W	137	5.7	1B	(1)
10	July 21, 1966	17.85°S	178.56°W	589	5.6	1B	(1)
11	Dec. 01, 1966	14.03°S	167.04°E	136	6.0	1B	(1)
12	Feb. 03, 1967	5.58°S	110.53°E	543	5.5	1B	(1)
13	Mar. 24, 1967	6.01°S	112.33°E	606	5.9	1A	(1)
14	Oct. 09, 1967	21.14°S	179.16°W	607	6.2	1A	(2)
15	Nov. 14, 1967	5.46°S	147.05°E	194	5.6	1B	(1)
16	Dec. 01, 1967	49.45°N	154.40°E	144	5.9	1B	(1)
17	Dec. 27, 1967	21.29°S	68.20°W	91	6.3	1A	(1)
18	Jan. 07, 1968	5.08°S	153.88°E	118	5.5	1B	(1)
19	Nov. 04, 1968	14.20°S	172.02°E	596	5.8	1B	(1)
20	Mar. 30, 1972	25.77°S	179.61°E	485	6.1	1A	(2)
21	Nov. 08, 1974	42.60°N	141.86°E	122	5.9	1B	(2)
22	Feb. 22, 1975	24.97°S	178.88°W	338	6.1	1B	(2)

(1)=Oike¹⁹⁶¹; (2)=This study.

attention to the temporal change in stress due to S wave. There remains still a question whether or not the second shock occurs during the stress disturbance due to S wave pulse. To answer the question we shall compute the stress field generated from the first shock in the next paragraph, in which the amount of the stress disturbance which trigger the second shock will also be estimated.

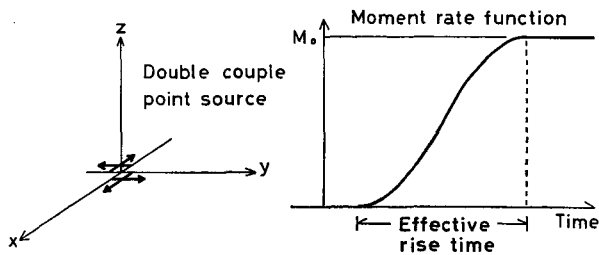


Fig. 53 (a) Double-couple point source and coordinate system used in the calculation. (b) Moment rate function assumed.

Strain seismograms

In order to obtain the stress change due to the first shock, we computed the strain seismograms. Here a double-couple point source with the moment rate function $M(t)$ was assumed (Fig. 53(a)). Since $l > L^*$ for TYPE 2B, this assumption seems to be valid. The method of computation of the strain seismograms generated from the double-couple point source in an infinite homogeneous medium has been given by Sasatani and Kasahara¹⁰⁸).

The moment rate function was assumed as follows:

$$\begin{aligned} M(t)/M_0 &= \frac{2}{\tau_e^2} t^2 && \text{for } 0 \leq t \leq \frac{\tau_e}{2} \\ &= 1 - \frac{2}{\tau_e^2} (\tau_e - t)^2 && \text{for } \frac{\tau_e}{2} \leq t \leq \tau_e \\ &= 1 && \text{for } \tau_e \leq t \end{aligned}$$

where τ_e is the effective rise time which may represent the duration of the faulting (Fig. 53(b)). The effective rise time was calculated by L^*/V_r . This seems to be valid because the term L^*/V_r is roughly equivalent to the total duration of faulting for earthquakes with rapid rise time of slip dislocation (Kanamori and Anderson⁶⁹). L^* was estimated by equation (20) or Fig. 51 and V_r was taken as 4.0–4.5 km/sec from Fig. 32.

Sasatani and Kasahara¹⁰⁸) analyzed the strain seismograms recorded at the Erimo Geophysical Observatory for near earthquakes and showed that the assumed source model is valid as a first approximation.

If the focal mechanism solution, the seismic moment and the effective rise time are given for the first shock, then the dynamic strain field (strain seismogram) at the place where the second shock occurs can be calculated. The most important stress in the double-couple force system is the shear stress τ_{xy} in the coordinate system used (see Fig. 53 (a)). This stress is calculated from the relation $\tau_{xy} = \mu \epsilon_{xy}$, where μ is the rigidity. If the focal mechanism solution for the second shock is different from that for the first shock, $\tau_{xy}(\epsilon_{xy})$ obtained above must be transformed into $\tau'_{xy}(\epsilon'_{yx})$ appropriate to the solution for the second shock by the change of axes (Jaeger and Cook¹⁰⁹).

Strain seismograms generated from the first shock were computed for the multiple shocks classified into TYPE 2B. Figure 54 shows the ϵ_{xy} component of the strain seismograms. This figure clearly shows that the stress disturbance (the upward motion represents the stress increase) is very large within the time of the S wave arrival. The time of occurrence of the second shock is also

denoted in the figure by an arrow. The ambiguity in determining the time of occurrence of the second shock is probably ± 1.0 sec that results from the accuracy of estimation of the apparent rupture velocity. Although we have such ambiguity in that time, it is safely said that the second shock occurred during the stress disturbance due to S wave pulse and was triggered by S wave. The stress increase due to S wave pulse is estimated to be several bars at most. The stress required to trigger earthquakes is smaller by about two order of magnitude than the stress drop of deep-focus earthquakes. Since the second shock for multiple shocks 2, 5, 13 and 14 occurred in a few second after the arrival of S wave, these multiple shocks might be classified into TYPE 1B. The dynamic stress change, however, is much larger than the static stress change for these earthquakes as shown in Fig. 54. Therefore, these multiple shocks may be considered as a delayed response to the stress change due to S wave pulse.

3.4 Discussion

The rupture process may be considered that rupture starting at a point where the concentrated stress exceeds the material strength propagates with a rupture velocity lower than S wave velocity and stops at a point where the concentrated stress at a crack tip is lower than the material strength. In connection with this rupture process, Yamashita⁶¹⁾ showed in his numerical experiments that the inhomogeneous initial stress field is more important in a dynamic process of fault motion. He also showed that the rupture pattern, the distribution of the dislocation, and the stress change before and after the generation of a fault are closely related to this inhomogeneous initial stress. His experiment suggests that the various types of deep multiple shocks are closely related to the distribution of the initial stress and the material strength.

We discuss the mechanism of a doublet in one dimension for simplicity. Two stress concentrations must be exist in the initial stress field to generate a multiple shock, a doublet: one of these is very close to the material strength and the other, somewhat lower than the material strength. It is assumed that the material strength is constant everywhere. Depending on the distribution of the inhomogeneous initial stress and on the stress disturbance due to the first shock, the various types of multiple shocks are able to occur. Based on the study of Yamashita⁶¹⁾, a schematic illustration of the stress field corresponding to each type is shown in Fig. 50. The dashed line in the figure is the

inhomogeneous initial stress and the full line, the stress disturbance due to the first shock.

The rupture mechanism of multiple shocks can be interpreted as follows. TYPE 1A: Immediately after the main shock occurs under the stress field shown by the dashed line, the stress field will change into that shown by the full line (Fig. 50). The stress at the end of the main shock fault is very close to the material strength, but is not enough to generate new rupture yet. As tectonic stress increases with time, the stress continuously reaches the material strength at that point, exceeds that strength, and follows the second shock that is observed as aftershocks. TYPE 1B: The stress concentration due to the main shock occurs apart from the main shock fault depending on the distribution of the initial stress which is different from that for TYPE 1A. As tectonic stress increases, aftershocks occur there. TYPE 2A: The initial stress field may be similar to that for TYPE 1A, but the second stress concentration is more close to the material strength than for TYPE 1A. Therefore the stress disturbance due to the rupture propagation of the first shock can directly trigger the second shock. TYPE 2B: There are two stress concentrations in the initial stress field which are very close to the material strength. Since the regions of stress concentration are considerably separated from each other, the second shock can not be triggered by the stress disturbance due to the rupture propagation of the first shock, but it can be triggered by the stress disturbance due to S wave pulse propagated from the first shock.

Recently Das and Aki⁶⁹⁾ proposed the barrier model, in which barriers are expressed by high values of material strength relative to tectonic stress, as a physical mechanism of multiple shocks. This barrier model may be physically equivalent to our model which has inhomogeneous initial stress under a constant material strength. Das and Aki stated that the lack of aftershocks in deep-focus earthquakes may be due to the homogeneity of material strength along the plane of rupture. However, the present study shows that the stress field or material strength in a region around the focus of these earthquakes is so inhomogeneous that the multiple shocks occur frequently.

The rupture mechanism of deep multiple shocks presented here assumes that the stress field in a region around the focus is inhomogeneous, and that the stress concentration is quite localized and interspersed. This assumption may be consistent with the relatively small source area of deep-focus earthquakes as obtained in section 2.4.

4. Summary of conclusions

The following results may be drawn from the present study.

(1) From the aftershock distribution, as well as through the analyses of seismic body waves in the time domain, we confirm that the kinematic source model of deep-focus earthquakes is the shear faulting.

(2) The aftershocks are located near the steeply dipping nodal plane of the mechanism solution of the main shock. This nodal plane is taken as the actual fault plane of the main shock.

(3) The stress drop of deep-focus earthquakes being larger than that of shallow earthquakes increases with focal depths. The average stress drop in a given depth range is 60 ± 30 bars for $0 < h < 50$ km, 160 ± 45 bars for $100 < h < 200$ km, and 520 ± 270 bars for $300 < h < 650$ km.

(4) The rupture velocity of deep-focus earthquakes is less than S wave velocity V_s in a region around the focus, that is, about 80% of V_s .

(5) The source dimension of a single deep-focus earthquake is 20 to 30 km at most, which is the size indicating that the stress concentration at the focus is quite limited in space.

(6) The sense of fault movements during earthquakes is consistent with the sense of deformation of the descending lithosphere in the Tonga arc. This indicates that the plastic deformation of the lithosphere may result from the fault movements during earthquakes.

(7) The multiple shocks with a remarkably short time interval occur very frequently in the deep seismic zone without showing regional characteristics.

(8) The multiple shocks can be classified into the following four types depending on the relative location, the apparent rupture velocity and the source dimension of the first shock. TYPE 1A: Aftershocks occurring near the fault plane of the main shock. TYPE 1B: Aftershocks occurring apart from the fault plane of the main shock. TYPE 2A: The multiple shock triggered by the rupture propagation of the first shock. TYPE 2B: The multiple shock triggered by S wave radiated from the first shock. For occurrence of these multiple shocks, TYPE 1B and TYPE 2B are the frequent types.

(9) The distribution of the initial stress and material strength plays an important role in the process of the multiple shocks. The inhomogeneous initial stress, under which the multiple shocks occur, indicates that the stress concentration at the focus is quite limited in space. This is consistent with (5).

(10) For the multiple shocks of TYPE 2B, the stress disturbance due to S wave pulse that can trigger the subsequent shock amounts to several bars at most. In other words, the earthquake with the stress drop of several hundred bars can be triggered by the stress disturbance of several bars.

Acknowledgements: The author wishes to express his deepest gratitude to Professor Hiroshi Okada for critically reading the manuscript and for giving many valuable suggestions. I also thank Professor Kyozi Tazime, and Drs. Hideki Shimamura and Katsuyuki Abe for their continuous encouragement during this study. Dr. Katsuyuki Abe gave me his program for computing the dynamic near-field displacement based on the Haskell model. I am grateful to Dr. Ken Sudo for his generosity in letting the author use his latest result before publication. Thanks are due to many colleagues in the Hokkaido University for helpful discussions.

The numerical computations were carried out by FACOM 230-75 at the Hokkaido University Computing Center.

This paper is part of the author's doctoral thesis submitted to the Hokkaido University in March, 1979.

References

- 1) WADATI, K.: On the activity of deep-focus earthquakes in the Japan Island and neighbourhood. *Geophys. Mag.*, **8**, (1935), 305-326.
- 2) HONDA, H.: *The seismic waves*. 230 pp, Iwanami, Tokyo, (1954).
- 3) GUTENBERG, B. and C.F. RICHTER: *Seismicity of the Earth and Associated Phenomena*. 310 pp, Princeton University Press, Princeton, N.J., (1954).
- 4) SYKES, L.R.: The seismicity and deep structure of island arcs. *J. Geophys. Res.*, **71**, (1966), 2981-3006.
- 5) KATSUMATA, M.: Seismicity and some related problems in and near the Japanese Islands. *Kenshinjiho (Quat. J. Seismol.)*, **35**, (1970), 75-142 (in Jap.).
- 6) UTSU, T.: Seismological evidence for anomalous structure of island arcs with special reference to the Japanese region. *Rev. Geophys. Space Phys.*, **9**, (1971), 839-890.
- 7) UTSU, T.: Distribution of earthquake hypocenters in and around Japan. *Kagaku (Science)*, Iwanami Shoten, Tokyo, **44**, (1974), 739-746 (in Jap.).
- 8) UTSU, T.: Anomalies in seismic wave velocity and attenuation associated with a deep earthquake zone, 1. *J. Fac. Sci. Hokkaido Univ., Ser. 7 (Geophys.)*, **3**, (1967), 1-25.
- 9) OLIVER, J. and B. ISACKS: Deep earthquake zones, anomalous structure in the upper mantle, and the lithosphere. *J. Geophys. Res.*, **72**, (1967), 4259-4275.
- 10) ISACKS, B., J. OLIVER, and L.R. SYKES: Seismology and the new global tectonics. *J. Geophys. Res.*, **73**, (1968), 5855-5899.
- 11) ISACKS, B. and P. MOLNAR: Distribution of stresses in the descending lithosphere from a global survey of focal-mechanism solutions of mantle earthquakes. *Rev.*

- Geophys. Space Phys., **9**, (1971), 103-174.
- 12) HONDA, H.: Earthquake mechanism and seismic waves. *J. Phys. Earth*, **10**, (1962), 1-97.
 - 13) STAUDER, W. and G.A. BOLLINGER: The S-wave project for focal mechanism studies, earthquakes of 1962. *Bull. Seis. Soc. Am.*, **54**, (1964), 2199-2208.
 - 14) ICHIKAWA, M.: Reanalyses of mechanism of earthquakes which occurred in and near Japan, and statistical studies on the solutions obtained, 1926-1968. *Geophys. Mag.*, **35**, (1971), 207-274.
 - 15) AKI, K.: Generation and propagation of G waves from the Niigata earthquake of June 16, 1964. Part 2. Estimation of earthquake moment, released energy, and stress strain drop from the G wave spectrum. *Bull. Earthq. Res. Inst.*, **44**, (1966), 73-88.
 - 16) KANAMORI, H.: Synthesis of long-period surface waves and its application to earthquake source studies: Kurile Islands earthquake of October 13, 1963. *J. Geophys. Res.*, **75**, (1970), 5011-5027.
 - 17) KANAMORI, H.: Mode of strain release associated with major earthquakes in Japan. *Ann. Rev. Earth Planet. Sci.*, **1**, (1973), 213-239.
 - 18) ABE, K.: Focal process of the south Sandwich islands earthquake of May 26, 1964. *Phys. Earth Planet. Interiors*, **5**, (1972), 110-122.
 - 19) ABE, K.: Tsunami and mechanism of great earthquakes. *Phys. Earth Planet. Interiors*, **7**, (1973), 143-153.
 - 20) ABE, K.: Fault parameters determined by near- and far-field data: The Wakasa Bay earthquake of March 26, 1963. *Bull. Seis. Soc. Am.*, **64**, (1974), 1369-1382.
 - 21) TENG, T.L. and A. BEN-MENACHEM: Mechanism of deep earthquakes from spectrums of isolated body-wave signals. *J. Geophys. Res.*, **70**, (1965), 5157-5170.
 - 22) BERCKHEMER, H. and K.H. JACOB: Investigation of the dynamic process in earthquake foci by analyzing the shape of body waves. *Proc. Xth Assembly. ESC II*, (1968), 253-352.
 - 23) BOLLINGER, G.A.: Determination of earthquake fault parameters from long-period P waves. *J. Geophys. Res.*, **73**, (1968), 785-807.
 - 24) KHATTRI, K.: Body wave directivity functions for two dimensional fault model and kinematic parameters of a deep focus earthquake. *J. Geophys. Res.*, **77**, (1972), 2062-2071.
 - 25) MIKUMO, T.: Long-period P waveforms and the source mechanism of intermediate earthquakes. *J. Phys. Earth*, **17**, (1969), 169-192.
 - 26) MIKUMO, T.: Source process of deep and intermediate earthquakes as inferred from long-period P and S waveforms. 1. Intermediate depth earthquakes in the southwest Pacific region. *J. Phys. Earth*, **19**, (1971) 1-19.
 - 27) MIKUMO, T.: Source process of deep and intermediate earthquakes as inferred from long-period P and S waveforms. 2. Deep-focus and intermediate earthquakes around Japan. *J. Phys. Earth*, **19**, (1971), 303-320.
 - 28) CHANDRA, U.: Source processes of a large deep-focus earthquake and its tectonic implications - The Western Brazil earthquake of 1963: Comments. *Phys. Earth Planet. Interiors*, **7**, (1973), 115-121.
 - 29) FUKAO, Y.: Focal process of a deep-focus earthquake as deduced from long-period P and S waves. *Bull. Earthq. Res. Inst.*, **48**, (1970), 707-727.
 - 30) FUKAO, Y.: Source process of a large deep-focus earthquake and its tectonic implications - The western Brazil earthquake of 1963. *Phys. Earth Planet. Interiors*, **5**, (1972), 61-76.
 - 31) WYSS, M.: Stress estimates for south American shallow and deep earthquakes. *J. Geophys. Res.*, **75**, (1970), 1529-1544.

- 32) WYSS, M. and P. MOLNAR: Source parameters of intermediate and deep focus earthquakes in the Tonga arc. *Phys. Earth Planet. Interiors*, **6**, (1972), 279-292.
- 33) LINDE, A.T. and I.S. SACKS: Dimensions, energy, and stress release for south American deep earthquakes. *J. Geophys. Res.*, **77**, (1972), 1439-1451.
- 34) KOYAMA, J.: Source process of Vladivostok deep focus earthquake of September 10, 1973. *Sci. Rep. Tohoku Univ., Ser. 5, Geophysics*, **23**, (1975), 83-101.
- 35) KOYAMA, J.: Seismic moment of the Vladivostok deep-focus earthquake of September 29, 1973, deduced from P waves and mantle Rayleigh waves. *Phys. Earth Planet. Interiors*, **16**, (1978), 307-317.
- 36) SASATANI, T.: Source process of a deep-focus earthquake in the Sea of Okhotsk as deduced from long-period P and S waves. *J. Phys. Earth*, **22**, (1974), 279-297.
- 37) SASATANI, T.: Source process of a large deep-focus earthquake of 1970 in the Sea of Okhotsk. *J. Phys. Earth*, **24**, (1976), 27-42.
- 38) MOGI, K.: Some discussion on aftershocks, foreshocks and earthquake swarms — The fracture of a semi-infinite body caused by an inner stress origin and its relation to earthquake phenomena (Third paper). *Bull. Earthq. Res. Inst.*, **41**, (1963), 615-658.
- 39) MIYAMURA, S., S. OMOTE, R. TEISSEYRE and E. VESANEN: Multiple shocks and earthquake series pattern. *Bull. Int. Inst. Seis. Earthquake Eng.*, **2**, (1965), 71-92.
- 40) ISACKS, B., L.R. SYKES, and J. OLIVER: Spatial and temporal clustering of deep and shallow earthquakes in the Fiji-Tonga-Kermadec region. *Bull. Seis. Soc. Am.*, **57**, (1967), 935-958.
- 41) OIKE, K.: The deep earthquake of June 22, 1966 in the Banda Sea: A multiple shock. *Bull. Disas. Prev. Res. Inst., Kyoto Univ.*, **19**, (1969), 55-65.
- 42) GUPTA, H.K. and B.K. ROSTOGI: Earthquake m_b vs M_s relations and source multiplicity. *Geophys. J. R. astr. Soc.*, **28**, (1972), 65-89.
- 43) FUKAO, Y. and M. FURUMOTO: Foreshocks and multiple shocks of large earthquakes. *Phys. Earth Planet. Interiors*, **10**, (1975), 355-368.
- 44) CHUNG, WAI-YING and H. KANAMORI: Source process and tectonic implications of the Spanish deep-focus earthquake of March 29, 1954. *Phys. Earth Planet. Interiors*, **13**, (1976), 85-96.
- 45) JEFFREYS, H.: *The Earth*, 4th Edition, Cambridge University Press, 1962.
- 46) HODGSON, J.H. and R.S. STOREY: Tables extending Byerly's fault plane techniques of any focal depth. *Bull. Seis. Soc. Am.*, **43**, (1953), 49-61.
- 47) SATO, R.: Attenuation of seismic waves. *J. Phys. Earth*, **15**, (1967), 32-61.
- 48) MIKUMO, T. and T. KURITA: Q distribution for long-period P waves in the earth. *J. Phys. Earth*, **16**, (1968), 11-29.
- 49) HASKELL, N.A.: Crustal reflection of plane SH waves. *J. Geophys. Res.*, **65**, (1960), 4147-4150.
- 50) HASKELL, N.A.: Crustal reflection of plane P and SV waves. *J. Geophys. Res.*, **67**, (1962), 4751-4765.
- 51) HAGIWARA, T.: A note on the theory of the electromagnetic seismograph. *Bull. Earthq. Res. Inst.*, **36**, (1958), 139-164.
- 52) HASKELL, N.A.: Total energy and energy spectral density of elastic wave radiation from propagating faults. *Bull. Seis. Soc. Am.*, **54**, (1964), 1811-1841.
- 53) HASKELL, N.A.: Elastic displacements in the near-field of a propagating fault. *Bull. Seis. Soc. Am.*, **59**, (1969), 865-908.
- 54) HIRASAWA, T. and W. STAUDER, S.J.: On the seismic body waves from a finite moving source. *Bull. Seis. Soc. Am.*, **55**, (1965), 237-262.
- 55) SAVAGE, J.C.: The effect of rupture velocity upon seismic first motions. *Bull. Seis. Soc. Am.*, **55**, (1965), 263-275.

- 56) SAVAGE, J.C.: Radiation from a realistic model of faulting. *Bull. Seis. Soc. Am.*, **56**, (1966), 577-592.
- 57) SASATANI, T.: Source process of earthquakes as deduced from long-period seismic body waves. 2. Intermediate-depth earthquakes in the southern Kurile island arc. *Geophys. Bull. Hokkaido Univ.*, **31**, (1974), 59-81 (in Jap.).
- 58) MARUYAMA, T.: On the force equivalents of dynamic elastic dislocations with reference to the earthquake mechanism. *Bull. Earthq. Res. Inst.*, **41**, (1963), 467-486.
- 59) BURRIDGE, R. and L. KNOPOFF: Body force equivalents for seismic dislocations. *Bull. Seis. Soc. Am.*, **54**, (1964), 1875-1888.
- 60) ESHELBY, J.D.: The determination of the elastic field of an ellipsoidal inclusion and related problems. *Proc. Roy. Soc., London*, **A241**, (1975), 376-396.
- 61) YAMASHITA, T.: On the dynamical process of fault motion in the presence of friction and inhomogeneous initial stress, Part 1. Rupture propagation. *J. Phys. Earth*, **24**, (1976), 417-444.
- 62) AUER, F. and H. BERCKHEMER: Deep focus earthquakes as triggered dislocation processes. *Phys. Earth Planet. Interiors*, **6**, (1972), 300-305.
- 63) DAS, S. and K. AKI: Fault plane with barriers: A versatile earthquake model. *J. Geophys. Res.*, **82**, (1977), 5658-5670.
- 64) DAVIES, D. and B.R. JULIAN: A study of short period P wave signals from Longshot. *Geophys. J.R. astr. Soc.*, **29**, (1972), 185-202.
- 65) SLEEP, N.H.: Teleseismic P-wave transmission through slabs. *Bull. Seis. Soc. Am.*, **63**, (1973), 1349-1373.
- 66) SASATANI, T.: Study of the source process of deep-focus earthquakes. Ph. D. Thesis, Hokkaido Univ., (1979), pp 1-234.
- 67) OIKE, K.: Distribution of stresses and dynamic displacements around a fault. *Zisin (J. Seis. Soc. Jap.)*, **24**, (1971), 318-334 (in Jap.).
- 68) RYBICKI, K.: Analysis of aftershocks on the basis of dislocation theory. *Phys. Earth Planet. Interiors*, **7**, (1973), 409-422.
- 69) KANAMORI, H. and DON. L. ANDERSON: Theoretical basis of some empirical relations in seismology. *Bull. Seis. Soc. Am.*, **65**, (1975), 1073-1095.
- 70) ABE, K.: Reliable estimation of the seismic moment of large earthquakes. *J. Phys. Earth*, **23**, (1975), 381-390.
- 71) GELLER, R.J.: Scaling relation for earthquake source parameters and magnitudes. *Bull. Seis. Soc. Am.*, **66**, (1976), 1501-1523.
- 72) SASATANI, T.: Source process of earthquakes as deduced from long-period seismic body waves. 1. Distortion of long-period P waveforms. *Geophys. Bull. Hokkaido Univ.*, **29**, (1973), 1-16 (in Jap.).
- 73) KIRUCHI, M. and Y. FUKAO: Seismic return motion. *Phys. Earth Planet. Interiors.*, **12**, (1976), 343-349.
- 74) STRELITZ, R.A.: Seismic return motion - Comments. *Phys. Earth Planet. Interiors.*, **14**, (1977), 373-382.
- 75) BARAZANGI, M., W. PENNINGTON, and B. ISACKS: Global study of seismic wave attenuation in the upper mantle behind island arcs using pP waves. *J. Geophys. Res.*, **80**, (1975), 1079-1092.
- 76) OIKE, K.: On the nature of the occurrence of intermediate and deep earthquakes 3. Focal mechanisms of multiplets. *Bull. Disas. Prev. Res. Inst., Kyoto Univ.*, **21**, (1971), 153-178.
- 77) FUKAO, Y.: Seismological evidence for selectivity in slip planes under down-dip extension or compression. *Geofis. Internacional*, **13**, (1973), 223-242.
- 78) SAVAGE, J.C.: The mechanism of deep-focus faulting. *Tectonophysics*, **8**, (1969),

- 115-127.
- 79) RITSEMA, A.R.: The mechanism of mantle earthquakes in relation to phase transformation processes. *Phys. Earth Planet. Interiors*, **3**, (1970), 503-510.
 - 80) FURUMOTO, M.: Spacio-temporal history of the deep Colombia earthquake of 1970. *Phys. Earth Planet. Interiors*, **15**, (1977), 1-12.
 - 81) KANAMORI, H. and F. PRESS: How thick is the lithosphere. *Nature*, **226**, (1970), 330-331.
 - 82) YOSHII, T.: Regionality of group velocities of Rayleigh waves in the Pacific and thickening of the plate. *Earth Planet. Sci. Lett.*, **25**, (1975), 305-312.
 - 83) HANKS, T.C.: The Kurile trench-Hokkaido rise system: Large shallow earthquakes and simple models of deformation. *Geophys. J.R. astr. Soc.*, **23**, (1971), 173-189.
 - 84) WATTS, A.B. and M. TALWANI: Gravity anomalies seaward of deep-sea trenches and their tectonic implications. *Geophys. J.R. astr. Soc.*, **36**, (1974), 57-90.
 - 85) MIZOUE, M.: Variation of earthquake energy release with depth. *Bull. Earthq. Res. Inst.*, **45**, (1967), 679-709.
 - 86) BRUNE, J.N.: Tectonic stress and the spectra of seismic shear waves from earthquakes. *J. Geophys. Res.*, **75**, (1970), 4997-5009.
 - 87) LINDE, A.T., I.S. SACKS, and J.A. SNOKE: Multiple rupture earthquakes and the determination of source parameters. in *Carnegie Inst. Wash. Year Book*, **75**, (1976), 281-286.
 - 88) MANSINHA, L.: The velocity of shear fracture. *Bull. Seis. Soc. Am.*, **54**, (1964), 369-376.
 - 89) RICHARDS P.G.: Dynamic motions near an earthquake fault: A three-dimensional solution. *Bull. Seis. Soc. Am.*, **66**, (1976), 1-32.
 - 90) WU, F.T., K.C. THOMSON, and H. KUENZLER: Stick-slip propagation velocity and seismic source mechanism. *Bull. Seis. Soc. Am.*, **62**, (1972) 1621-1628.
 - 91) JOHNSON, T.L. and C.H. SCHOLZ: Dynamic properties of stick-slip friction of rock. *J. Geophys. Res.*, **81**, (1976), 881-888.
 - 92) SASATANI, T.: Mechanism of mantle earthquakes near the junction of the Kurile and the northern Honshu arcs. *J. Phys. Earth*, **24**, (1976), 341-354.
 - 93) ISACKS, B., L.R. SYKES, and J. OLIVER: Focal mechanisms of deep and shallow earthquakes in the Tonga-Kermadec region and the tectonics of island arcs. *Geol. Soc. Am. Bull.* **80**, (1969), 1443-1470.
 - 94) HERRIN, E.: Introduction to "1968 seismological tables of P phases". *Bull. Seis. Soc. Am.*, **58**, (1968), 1193-1241.
 - 95) JEFFREYS, H. and M. SHIMSHONI: The time of pP, sS, sP and pS. *Geophys. J.R. astr. Soc.*, **8**, (1963), 324-337.
 - 96) OIKE, K.: On the nature of the occurrence of intermediate and deep earthquakes 2. Spatial and temporal clustering. *Bull. Disas. Prev. Res. Inst., Kyoto Univ.*, **21**, (1971), 43-73.
 - 97) STRELITZ, R.: The September 5, 1970 Sea of Okhotsk earthquake: A multiple event with evidence of triggering. *Geophys. Res. Lett.*, **2**, (1975), 124-127.
 - 98) SUDO, K.: Study of deep focus earthquakes under the eastern border region of Peru. Unpublished data, (1976).
 - 99) SUDO, K.: Source process of a Bonin islands deep-focus earthquake of March 7, 1978. Unpublished data, (1978).
 - 100) RYALL, A. and W.U. SAVAGE: A comparison of seismological effects for the Nevada underground test Boxcar with natural earthquakes in the Nevada region. *J. Geophys. Res.*, **74**, (1969), 4281-4289.

- 101) GOUGH, D.I. and W.I. GOUGH: Load-induced earthquakes at lake Kariba - II. *Geophys. J.R. astr. Soc.*, **21**, (1970), 79-101.
- 102) RALEIGH, C.B., J.H. HEALY, and J.D. BREDHOEFT: Faulting and crustal stress at Rangely, Colorado; in *Flow and Fracture of Rocks*, *Geophys. Monogr. Ser.*, **16**, edited by H.C. HEARD, I.Y. BORG, N.L. CARTER, and C.B. RALEIGH, AGU, Washington, D.C., (1972), 275-284.
- 103) OHTAKE, M.: Seismic activity induced by water injection at Matsushiro, Japan. *J. Phys. Earth*, **22**, (1974), 163-176.
- 104) FLETCHER, J.B. and L.R. SYKES: Earthquakes related to hydraulic mining and natural seismic activity in western New York State. *J. Geophys. Res.*, **82**, (1977), 3767-3780.
- 105) POMEROY, P.W., D.W. SIMPSON, and M.L. SBAR: Earthquakes triggered by surface quarrying - The Wappingers falls, New York sequence of June, 1974. *Bull. Seis. Soc. Am.*, **66**, (1976), 685-700.
- 106) BRUNE, J.N.: Earthquake modeling by stick-slip along precut surface in stressed foam rubber. *Bull. Seis. Soc. Am.*, **63**, (1973), 2105-2119.
- 107) AKI, K.: Earthquake mechanism. *Tectonophysics*, **13**, (1972), 423-446.
- 108) SASATANI, T. and M. KASAHARA: Analyses of strain seismograms from near earthquakes. *Zisin (J. Seis. Soc. Jap.)*, **31**, (1978), 11-23 (in Jap.).
- 109) JAEGER, J.C. and N.G.W. COOK: *Fundamentals of Rock Mechanics*, 515 pp, Chapman and Hall, (1969).